

REPORT DOCUMENTATION PAGE

Form Approved
OMB No. 0704-0188

The public reporting burden for this collection of information is estimated to average 1 hour per response, including the time for reviewing instructions, searching existing data sources, gathering and maintaining the data needed, and completing and reviewing the collection of information. Send comments regarding this burden estimate or any other aspect of this collection of information, including suggestions for reducing the burden, to the Department of Defense, Executive Service Directorate (0704-0188). Respondents should be aware that notwithstanding any other provision of law, no person shall be subject to any penalty for failing to comply with a collection of information if it does not display a currently valid OMB control number.

PLEASE DO NOT RETURN YOUR FORM TO THE ABOVE ORGANIZATION.

1. REPORT DATE (DD-MM-YYYY) 01-31-2012		2. REPORT TYPE Final		3. DATES COVERED (From - To) 07-01-2008 to 01-31-2012	
4. TITLE AND SUBTITLE A SMART MICROWAVE VACUUM ELECTRON DEVICE (MVED) USING FIELD EMITTERS				5a. CONTRACT NUMBER	
				5b. GRANT NUMBER FA9550-08-1-0396	
				5c. PROGRAM ELEMENT NUMBER	
6. AUTHOR(S) Jim Browning John Chiasson SIn Ming Loo				5d. PROJECT NUMBER	
				5e. TASK NUMBER	
				5f. WORK UNIT NUMBER	
7. PERFORMING ORGANIZATION NAME(S) AND ADDRESS(ES) Boise State University Department of Electrical and Computer Engineering 1910 University Dr. Boise, ID 83725-2075				8. PERFORMING ORGANIZATION REPORT NUMBER	
9. SPONSORING/MONITORING AGENCY NAME(S) AND ADDRESS(ES) USAF, AFRL AF Office of Scientific Research 875 N. Randolph St., Room 3112 Arlington, VA 22203				10. SPONSOR/MONITOR'S ACRONYM(S) AFOSR, DEPSOR	
				11. SPONSOR/MONITOR'S REPORT NUMBER(S)	
12. DISTRIBUTION/AVAILABILITY STATEMENT Public Disclosure					
13. SUPPLEMENTARY NOTES					
14. ABSTRACT A Crossed-Field Amplifier and related components were designed and tested. The device did not show gain. The inability to achieve gain is believed to be related to two causes: insufficient beam current and backward wave modes from the slow wave circuit. ICEPIC modeling of the device showed issues with backward waves, but modifications to the circuit design and CFA operating parameters did not change performance. The field emission arrays intended for the experiment did not meet specifications, so alternative field emission cathodes were used. While these new cathodes provided more current, high voltage arcing problems have limited their use. The distributed cathode part of the program was very successful as electron hop funnels were demonstrated and modeled. The modeling effort has provided tremendous insight into secondary emission hopping mechanism. These results will be used for future work in not only hop funnels but also dielectric charging in high voltage vacuum devices.					
15. SUBJECT TERMS crossed-field amplifier, field emission, electron transport					
16. SECURITY CLASSIFICATION OF:			17. LIMITATION OF ABSTRACT	18. NUMBER OF PAGES	19a. NAME OF RESPONSIBLE PERSON
a. REPORT	b. ABSTRACT	c. THIS PAGE			Jim Browning
U	U	U	UU	37	19b. TELEPHONE NUMBER (Include area code) 208-426-2347

Contract/Grant Title: A Smart Microwave Vacuum Electron Device
(MVED) Using Field Emitters

Contract/Grant#: FA9550-08-1-0396

Reporting Period: 1 August, 2008 to 31 January, 2012

Dr. Jim Browning
Dr. Sin Ming Loo
Dr. John Chiasson
Boise State University
Boise, ID

Dr. Jack Watrous
NumerEx
Albuquerque, NM

January 31, 2012

ABSTRACT

A Crossed-Field Amplifier and related components were designed and tested. The device did not show gain. The inability to achieve gain is believed to be related to two causes: insufficient beam current and backward wave modes from the slow wave circuit. ICEPIC modeling of the device showed issues with backward waves, but modifications to the circuit design and CFA operating parameters did not change performance. The field emission arrays intended for the experiment did not meet specifications, so alternative field emission cathodes were used. While these new cathodes provided more current, high voltage arcing problems have limited their use. The distributed cathode part of the program was very successful as electron hop funnels were demonstrated and modeled. The modeling effort has provided tremendous insight into secondary emission hopping mechanism. These results will be used for future work not only in hop funnels but also dielectric charging in high voltage vacuum devices.

I. Introduction

The Smart MVED project is based on the use of gated vacuum field emitters as a distributed electron source. The vehicle for the smart control experiment is a 1 GHz linear format Crossed-Field Amplifier (CFA). A representation of the CFA concept is shown in Fig. 1. It consists of a meander line slow wave circuit, a cathode structure, electromagnets, an end collector, Field Emission Arrays (FEAs), and a control system. The cathode structure has slits through which electrons are injected into the interaction region. FEAs placed below the sole electrode provide the current and can be addressed to provide spatial control of the injected current. The system was tested in Years 1 and 2 and could not achieve gain. Several modifications were made including a new slow wave circuit design and materials as well as new cathodes. The device was also operated in an injected beam configuration rather than a distributed cathode configuration for the last 18 months of the project. As of January 31, 2012 gain was not achieved in the device. This report describes the efforts to achieve device operation in terms of the cathode, the slow wave circuit, the hop funnel configurations, and the simulations.

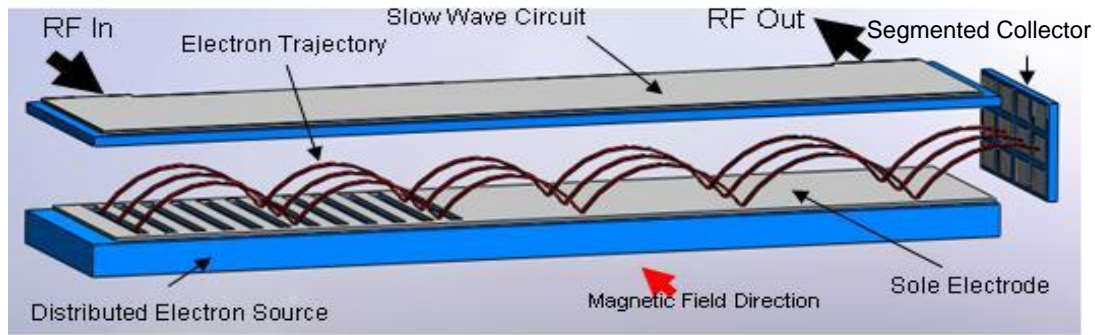


Figure 1. Smart CFA concept with distributed electron source, a meander line slow wave circuit, and a segmented end collector.

The CFA design was completed in year 1 but underwent extensive modifications. Although intended to operate near 1 GHz, the device has been tested at frequencies as low as 500 MHz. The original basic parameters are given in Table 1 below along with the actual test values. The system uses a sole electrode to fix the electric field and electromagnets to generate the magnetic field. The gap has been varied from 6 to 12 mm, and the slow wave circuit provides a factor of twenty retardation because of both geometric and dielectric properties depending upon type.

Table 1. CFA design specifications

CFA Parameter	Design Value	Actual
Center Frequency	1 GHz	0.5 to 1 GHz
Anode to Cathode Gap	6 mm	6 to 12 mm
Cathode Voltage	-3.1 kV	-2.5 to -4.2 kV
Magnetic Field	0.035 T	.02 to .04 T
Device Length	20 cm	
Circuit Width	2.7 cm	2.7 to 5 cm
Circuit Type	Meander line	
Beam Width	2.0 cm	2.0 cm
Injected Current	~0.2 A	< .005 A
RF Power Output	250 W	0
Expected Gain	>15 dB	0
Expected Efficiency	>50%	0

Because of cathode issues, the required current was never achieved. The maximum injected current was 5 mA well below the desired 200 mA. These issues are discussed in greater detail in the cathode section. The device was operated in the “distributed mode” and the “injected beam mode”. Neither achieved operation.

II. Cathode

A. Distributed Cathode Mode (Hop Funnel Mode)

The use of the FEAs has both advantages and disadvantages. The addressing and control provide the potential for dynamic feedback and even modulation at the operating frequency. However, FEAs are not reliable at high current and are sensitive to back bombardment. Hence, the original design had the FEAs placed below the sole electrode and out of the interaction space. To protect the emitters and to improve uniformity, a hop funnel configuration was used. In a hop funnel, electrons bombard a dielectric surface, secondary electrons are emitted, and the electrons “hop” along the funnel wall until they exit. This process can provide greatly improved beam uniformity from FEAs and have been successfully demonstrated to do so in Field Emission Displays. We have also tested hop funnels as part of this program development, and these results are presented later in this report.

The hop funnel concept requires that electrons bombard a dielectric surface and build up surface charge on that surface. An electrode biased positive at the top of the hop funnel pulls electrons to the exit. The secondary emission eventually creates a surface potential which results in unity gain of current, i.e. all injected current is extracted. Unity gain occurs at a high enough hop electrode bias, and the conditions depend upon the hop funnel geometry and dielectric surface conditions. The basic concept for this is shown in Fig. 2. This figure shows a hop funnel simulation using the 2D particle trajectory code Lorentz2E. In the model, primary electrons from FEAs bombard a funnel wall (shown in green). Secondary electrons are generated and followed until those electrons either strike

the funnel wall or exit. New secondaries are generated and followed. After all generations are followed, the net surface charge is calculated, and the new electric fields are calculated. A time step is advanced which determines the amount of deposited charge, and the process is repeated. The result is that for a large enough hop voltage, unity gain of current is achieved. As part of this program, the hop funnel has been built and tested and compared with the Lorentz simulation. These results are shown later in the report.

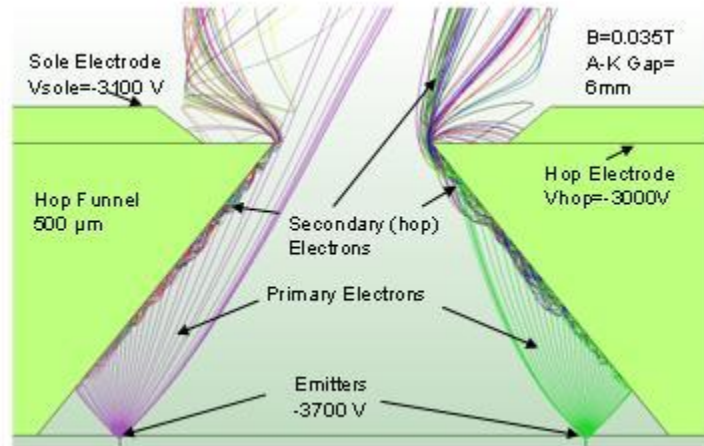


Figure 2. Hop funnel simulation using the Lorentz particle trajectory code.

To use the hop funnel concept in the CFA, it is necessary to avoid injection of primary electrons into the CFA interaction space and to form an optics system which allows only lower energy electrons to exit the sole slits. Otherwise, higher energy electrons will back bombard the sole electrode and be lost. This aspect is a major disadvantage of the hop funnel approach, but it is believed the improvement in uniformity of injection into the CFA will outweigh the inconvenience.

For the experiments in this project, the hop structure consists of three metal layers and two dielectric layers. The first metal layer is the interconnect layer for the connection lines. A picture of the metal 1 layer is shown in Fig. 3. This layer at the bottom of the structure consists of printed thick film silver on a 0.5 mm thick layer of LTCC. The metal lines connect to the field emission cathode address lines (gate and emitter) via an silver tape. A small piece of tape is placed at each pad. The sole and hop electrodes use a wrap around silver paste for connection. Also seen in Fig. 3 are the hop funnel slits. These slits are milled into the LTCC in its green state. The entrance slit is 0.9 mm and the exit is 0.3 mm. Then metal 1 is printed, and the structure is fired in an oven to burn out the binder. At this point, the LTCC can no longer be milled. For the hop funnel case a thin film aluminum layer (metal 2) is evaporated over the top of the plate to form the hop electrode. A carbon paste is placed in the slits and fired to remove the aluminum from the slits. The top of the electrode showing the exit slits with the aluminum is shown in Fig. 3. In addition, an ion mill is used to remove aluminum from the inside of the slits. Next, a dielectric paste (20 μm thick) is screen printed over the entire top of the structure to cover the top aluminum layer. Some of the paste flows into the slits and covers the edges of the aluminum. The structure is again fired to harden the dielectric paste. Because pin holes form in the dielectric paste, ion milling is again performed from the

top to remove any aluminum that may be exposed by the pin holes. The 3rd aluminum metal layer is now evaporated on top.

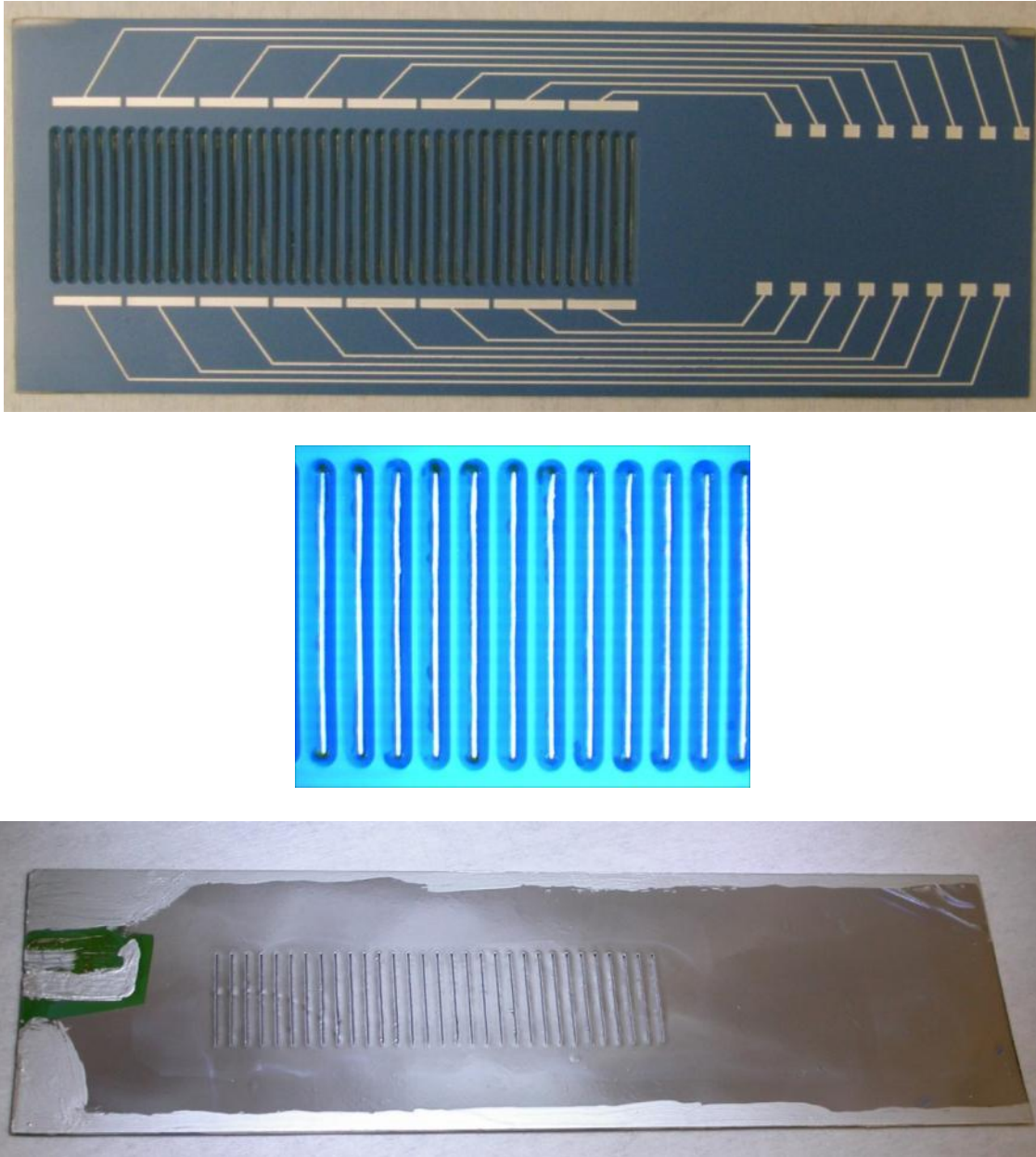


Figure 3. Underside of slit structure showing cathode connection lines (Top image), LTCC slits shown from the bottom of the structure (Middle image), and the top of the entire cathode structure showing the aluminum metal deposited over the slits (Bottom image).

Numerous experiments were performed with various versions of the slit structure. Although gain was never achieved, experiments did demonstrate that the beam could be extracted from the slits and that the electrons would cycloid down to the end of the structure when the magnetic field was applied. Hence, in CFA mode the distributed cathode structure with hop funnel worked as planned. As part of the structure testing, a

phosphor screen was placed over the slits as an anode. With the cathode biased negative, electrons were extracted out of the slits and onto the phosphor screen with no magnetic field. An image of the screen is shown in Fig. 4. The slits can be seen in the image as well as the uneven nature of the slit beams. This variation is due to the milling process which does not generate a uniform slit wall.

Arcing was a problem under the slit structure, so later hop funnel devices were modified. In the later devices, there was no “flat spot” between the bottoms of the slits. The slits were spaced so close together that when the slits were milled, the splits slightly overlapped leaving a sawtooth like configuration. This version greatly reduced charging/arcing problems underneath the hop funnel structure.

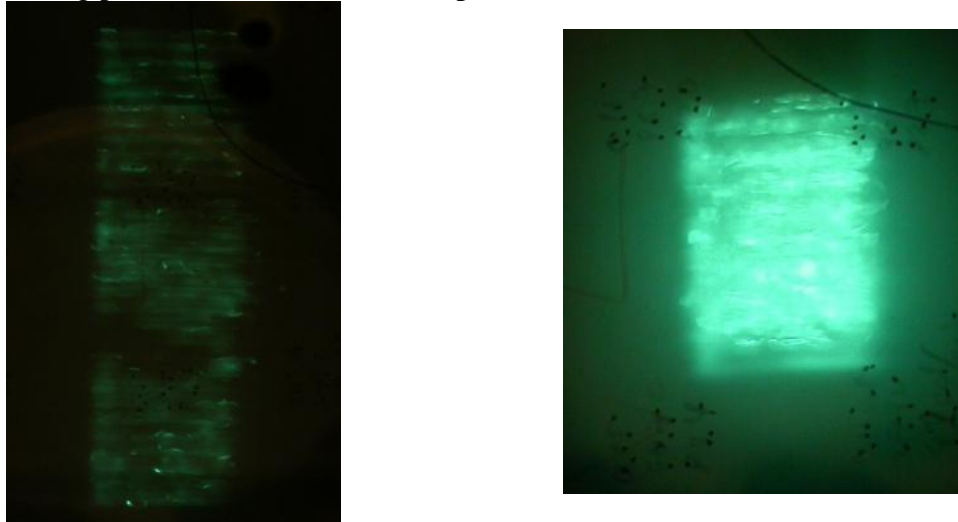


Figure 4. Images of a phosphor screen showing the electron pattern from the cathode hop funnel slit structure (Stellar cathode, Left and Pixtech cathode, Right)

B. Hop Funnel Simulation and Experiment

Lorentz2E has been used to simulate the CFA configuration and the hop funnel optics. These results are shown in Figures 2, 5, and 6. In Fig. 2, a close up of the structure is shown. FEAs are used to inject primary electrons which bombard the dielectric wall. Note that this hop funnel is a slit, but the simulation is 2D. The electrons hop along the walls drawn out by the hop electrode voltage. Then the electrons exit through the slit while some are reflected back by the sole electrode potential. The idea is seen in a larger view in Fig. 5. Here both the anode and cathode can be seen as well as the large cycloidal trajectories of the electrons which put the electrons near the slow wave circuit. Some electrons collected back on the sole electron while most continue on down the interaction space. A close up of the cycloidal turn point is shown in Fig. 6 where it can be seen that some electrons collect and others turn. Optimizing the electron optics to minimize or eliminate the collected electrons is a primary goal of the electron optics design.

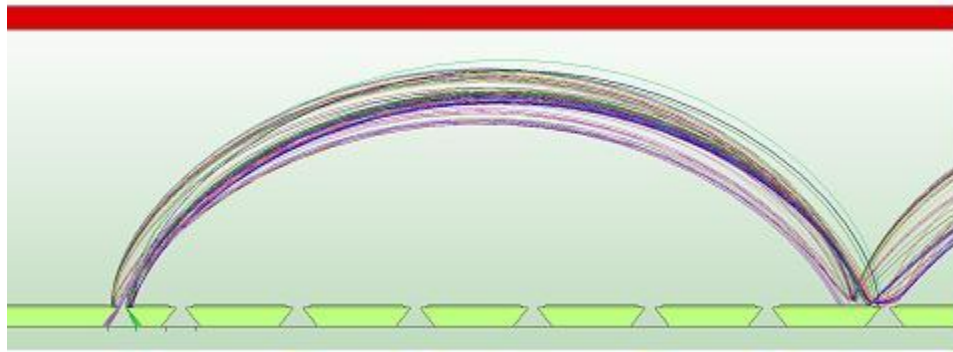


Figure 5. CFA configuration with the slow wave circuit and a cathode structure showing multiple possible slits for electron injection.

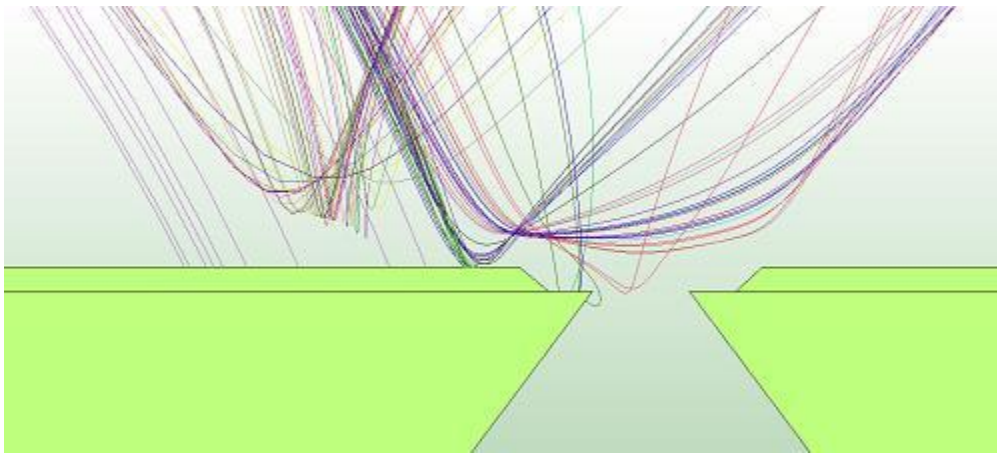


Figure 6. Simulation showing the cycloidal turn point for the electrons.

C. Injected Beam Mode

Because the CFA showed no gain with the distributed cathode/hop funnel configuration, the experiment was switched over to an injected beam mode. In this mode the experiments were operated with both Motorola and PixTech cathodes (described below). This injection setup is shown in Fig. 7 from the SIMION 3D particle trajectory simulation. SIMION is a simple Laplace Equation solver with particle tracking. However, since it is 3D and since no electron hopping needs to be simulated, it has allowed trajectory modeling of the CFA which is essentially a 3D structure. Modeling of the injected beam structure showed several problems which were observed experimentally. Initially, the sole electrode was fabricated with a “slot” at the beam entrance. This slot exposed the active area of the FE cathode. Some experimental results showed severe cathode arcing when the cathode was not covered. This problem is discussed later. However, the sole slot acted to defocus the electron beam and spread the beam out far greater than anticipated. This problem was not well understood until the modeling was completed. A new version of this configuration was then tested. In addition, the traditional magnetic diode test of the beam collection showed a strange variation. As the

magnetic field was increased, the current to the anode would decrease as expected. The current would transit the CFA and strike the end collector. However, as the field was increased further, the anode current would increase again. The problem, shown by the simulation, was that the electrons at the injection point were actually going over the anode electrode and creating two set of electron beams. Therefore, a “pusher” electrode was introduced at the entrance of the circuit to steer the beam into the interaction space. This electrode and the “no-slot” configuration greatly improved the beam injection. Finally, the beam spread shown by the SIMION modeling indicated a larger than expected loss along the magnetic field lines. End hats, which had been used prior, were improved and modeled to provide the minimum beam loss.



Figure. 7. SIMION simulation of the injected beam configuration of the CFA with the beam injection at right and the collector at left.

D. Cathode Types and Issues

Three type of field emission cathodes were used in this project. None exactly met the requirements of the project. These cathodes are briefly described here.

Stellar Lateral Emitters

The original program was based on receiving lateral, nano-layer carbon emitters from Stellar Micro Devices (SMD). Stellar had produced individual emitters that could produce nearly 50 times the required current density for this project. Particularly in the distributed cathode configuration, it was felt that such arrays could easily be fabricated. Initially, SMD provided parts from their ongoing projects. While these emitters were of the wrong shape and geometry for the CFA, they did allow testing. While individual emitters could provide high current, arrays of emitters were poor and would not come close to the requirements. In year 2, SMD fabricated emitters in the desired geometry based on our design/layout for the CFA. However, only two parts were ever delivered, and these parts had severe leakage and shorting. The parts were never used in the CFA system.

Motorola Spindt Emitters

Dr. Babu Chalamala provided some old Motorola FEAs for their display program. These emitters were molybdenum Spindt type on 2"x2" substrates. The parts were acceptable, but since many were old test parts, the leakage current was high. These parts were used in the CFA injected beam configuration, but the injected current never exceeded 1 mA. Part

of the issue included arcing problems which are discussed later. These cathodes were tested in year 2 of the project.

PixTech Display Spindt Emitters

Old 5.2” Field Emission Displays from PixTech were made available for this project. However, the displays were sealed, so the packages had to be broken open to expose the cathodes. This process often damaged the cathodes and increased gate to emitter leakage. In addition, the cathodes are much wider than the CFA structure, so part of the emitter area was exposed with no electrode over the top. In this mode, severe arcing would occur when the magnetic field was applied. These issues are discussed later. A new cathode fixture was developed, but several iterations on the design were needed to prevent the arcing, and the process is still ongoing. Nevertheless, these cathodes have allowed the largest injection current (7.5 mA) to date. The work to prevent arcing is still ongoing, and we will continue to use the few remaining PixTech cathodes for our CFA work.

Arcing and Leakage

One of the most prevailing issues seen throughout the project was arcing on the cathode. The CFA design and configuration have been continuously modified to reduce arcing on the cathode. The largest source of arcing was due to electron/ion back bombardment when the device was used in a crossed-field configuration. The source and results of the crossed field arcing will be discussed in more detail later in this report. Arcing on the cathode usually resulted in a degradation of the cathode’s performance and an increase in the leakage current. When arcing was observed, effort was placed on improving the CFA structure to prevent future arcing. However, as a result of repeated arc damage it became necessary to replace the cathode with a ‘new’ cathode. When a cathode was replaced it had to be properly setup which included burn in of the array (as they have been up to air for an extended period of time) and determining a section of the cathode capable of producing the necessary current. To find usable sections, a phosphor screen was often used to determine locations of emission. Once a section was found, the phosphor screen was switched to copper anode and finally tested in full structure for additional arcing issues. Leakage current in the cathodes have been a very large problem. With an increased leakage both the heat of the cathode and voltage drop across components is increased. The larger voltage drop caused by the leakage current results in a reduced gate to emitter voltage which, therefore, decreases the emission of the field emitters. The increase in heat further decreases performance of the field emitter arrays.

There have also been many attempts to repair ‘damaged’ cathodes. A variety of techniques have been used including cutting addressing lines, reverse biasing unused lines, and using voltage pulsing to blow shorted connection and spurious emission sites. However, all of these techniques have had very limited success in improving the performance of damaged cathodes.

III. Slow wave Circuit

A. LTCC Meander Line

The first slow wave circuit was a meander line based structure using Low Temperature Co-fired Ceramic (LTCC) as the dielectric and thick film silver as the conductor. The circuit was designed for a $50\ \Omega$ impedance, and measurements of the circuit show that the impedance is well match around the operating frequency with a cut off around 1.15 GHz. Loss was less than 2 dB at 1 GHz. The measured retardation was 18 rather than the predicted 20 partly due to a process non-uniformity (line width). A picture of the circuit is shown in Fig. 8. Note that a serious concern was charge build up on the dielectric. This circuit was tested with both the distributed cathode and injected beam cathode configuration. Neither case showed gain. The belief was that there was charging on the dielectric since the metal line is very thin. Therefore, a new circuit was fabricated as explained below.

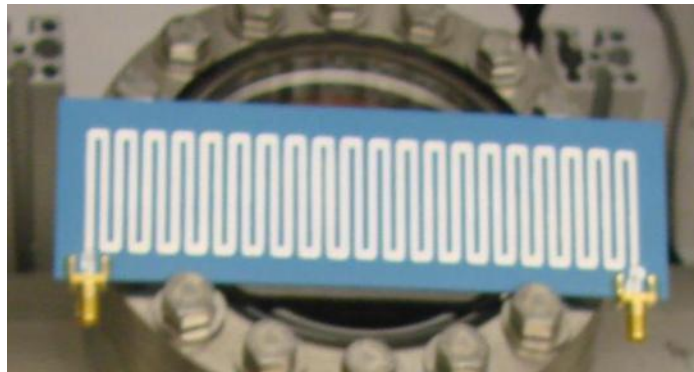


Figure 8. Meander line slow wave circuit on LTCC with SMA connectors

B. Copper Wire on Teflon

Based on prior CFA work, a wire type meander circuit was fabricated. This circuit used a flat narrow copper meander line cut from a copper plate using a water jet cutting system. The copper wire was then placed on a teflon dielectric and an aluminum back plane. The thicker copper wire and narrower pitch were designed to minimize charging between the metal on the dielectric. Note that the electron beam is much narrower (50%) than the circuit width. Several versions of this circuit were built primarily to adjust the alignment of the SMA connectors from horizontal to vertical to the circuit plane. This change allowed implementation of closer end hats. The new design also improved height adjustability allowing the CFA to be tested for a variety of gap distances. A picture of this new slow wave circuit is shown in Fig. 9.

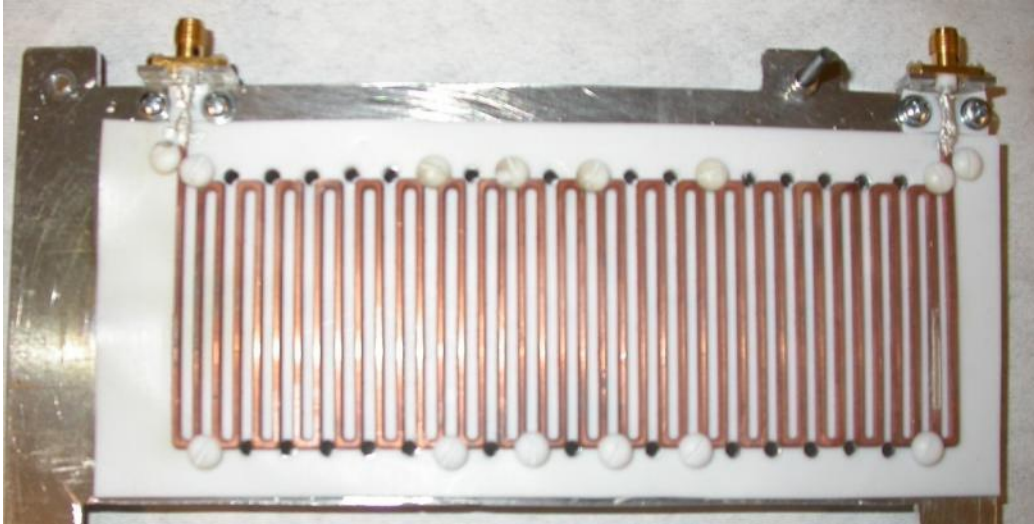


Figure 9. Copper meander line slow wave circuit on a Teflon dielectric

An additional slow wave circuit has also been designed. The new slow wave design has been created to have a larger retardation and increased cutoff to operating frequency ratio. It is believed that by increasing the cutoff frequency and reducing the operating frequency the magnitude of backward wave modes will be reduced. These backward waves may cause interference with the operation of the device. By using a larger retardation value, the slow wave phase velocity is decreased allowing a lower E/B drift velocity. By reducing the drift velocity the device is able to run at a lower cathode potential reducing the risk of high voltage arcing. This new slow wave circuit will be similar to the slow wave shown in Fig. 9 as it will also use a copper meander line on a Teflon dielectric.

IV. System Operation and Issues

A. Beam Injection and Arcing

As previously stated, arcing on the cathode has created numerous issues with operation of the CFA. Arcing on the cathodes was most often seen when trying to operate the structure with a magnetic field. Because of the nature of using cathodes not configured for this application, a number of additional components had to be added to the structure to protect these cathodes. When the Pixtech cathodes were originally added to the CFA structure, problems arose due to the cathodes being wider than the original structure design. A wider cathode resulted in the sole electrode covering only a portion of the total cathode. This left a large portion of the cathode exposed which would experience arcing issues when the beam was bent due to the cycloiding electrons striking the exposed cathode.

The cycloiding electrons were making it to the exposed cathode region as a result of the previously mentioned issue of beam spread. It was expected that using an injected beam would have a very limited amount of beam spread. However, when operated the beam spread was always significant. To prevent beam spread additional electrodes, referred as

endhats, were added to the sides of the sole and biased negative with respect to the cathode to contain the electrons above the sole.

It is believed that another problem with the beam injection method is the configuration of the sole electrode with the Pixtech cathodes. Original beam injection setups placed a sole electrode above the cathode by using a thin dielectric layer (mylar) on top of the cathode and placing the sole electrode on the dielectric. While this configuration proved sufficient for the injected beam, the dielectric on the surface of the cathode began to breakdown and contaminate the cathode. To remove dielectric from the surface of the cathode, dielectric spacers were built and placed around the exterior of the cathode. These insulators then provided a mounting location to raise the sole above the surface of the cathode. However, because of the necessary height of the spacers, the sole was actually 1-2 mm above the cathode. It is believed that this increased height has become an additional source of issues. When a strong magnetic field is applied to the structure the electric field is not strong enough to pull the electrons onto the sole to allow cycloiding; instead the electrons simply cycloid underneath the sole plate. Experimental work shows that about 50% of the emitted current is not able to get above the sole plate at high magnetic fields. Ongoing efforts include designing an extracting/focusing electrode to improve concentration of electrons emitted into the tube.

B. RF Gain

Attempts to achieve gain were unsuccessful. Experiments were performed with the distributed cathode and the injected beam cathode. Experiments were also performed with the thin LTCC meander line and the copper wire meander line. Injection currents up to 5 mA were tried. The anode to cathode gap was varied from 6 mm to 12 mm. The frequency was varied from 500 MHz to 1 GHz. The cathode voltage and magnetic field were varied over a wide range of parameters while monitoring the RF output through a directional coupler. No indication of gain was observed. There are presently two theories for this cause:

1. Beam power – the original design goal was 180 mA of beam current at -3.1 kV. None of the cathodes can provide this current level particularly in the injected beam mode. Designs are in progress to reduce the beam arcing issues using the PixTech cathodes. These cathodes should be able to put out 20 mA. The belief is that the lack of beam power is limiting the beam-wave interaction. ICEPIC simulations are planned in the future to study the minimum required beam current.
2. Backward waves – ICEPIC simulations have indicated that the circuit design results in backward wave modes near the meander line. These modes may be breaking up any forward wave interactions. The anode–cathode gap was increased to keep the cycloidal beam farther from the anode. However, these experiments did not show gain either. A new slow wave circuit has been designed and is being fabricated. This new circuit moves the operating frequency farther from cutoff

and should reduce excitation of backward modes. Further ICEPIC and VORPAL simulations are planned to help with the design future circuits.

V. ICEPIC Simulation

Work on modeling the BSU CFA began in November of 2009 and concluded in December of 2011. The primary tool used for the modeling effort was the Air Force Research Laboratory three-dimensional parallel electromagnetic particle-in-cell code, ICEPIC (R.E. Peterkin, J. W. Luginsland, *Comp. Sci. Engin.*, **4**, 42 (2002)); ICEPIC calculations were augmented through simple theoretical calculations and reduced-physics numerical calculations. In the following, the primary issues dealt with by the modeling support effort will be summarized.

As described elsewhere in this report, one of the components of the linear CFA is the meander line (referred to in the following as “the line”). This line carries alternating current that along with the geometric design of the line and the dielectric backing, is intended to produce a harmonic travelling wave in the neighboring region. This sort of structure is a challenge to model with ICEPIC. ICEPIC is quite good at modeling the interaction of electromagnetic waves with resonant structures, slow wave structures, waveguides, antennae, and the interaction of electrons with waves confined and produced within such structures. But an isolated structure upon which is imposed an externally generated current in order to produce fields within the volume in which it is contained does not fit easily within the set of physics models and boundary conditions characteristically encountered. Fortunately, at the onset of this effort, NumerEx was encountering essentially identical challenges in several different projects (compact pulse forming line, non-linear transmission line, spiral antenna for the BSU ICP thruster). This convergence of simultaneous, nearly identical requirements was resolved by a single solution that allows a single conductor in conjunction with a ground plane, or two paired conductors without the ground plane, to be driven with an external voltage source. Figure 10 shows a view of the geometry of the meander line as used in this work. The simulation domain consists of a rectangular parallellepiped volume bounded on top and bottom by conductors, on upstream and downstream faces and left and right faces by wave-absorbing boundary conditions. From the bottom conduction moving up, the bottom conductor is the sole plate, above this is an empty volume that is the interaction region, above this is a thin region in which resides the meander line, above this is a layer of dielectric material, and above this is the top conductor surface. The ends of the line connect to small cylindrical conductors that pass through cylindrical holes in the top boundary plane of the simulation domain where they attach to boundary conditions appropriate for driving the specified current.

In order to facilitate comparison between experiment and calculation, a series of calculations was undertaken in which two different experimental configurations were considered. One uses the LTCC dielectric ($\epsilon = 7.8$, Figure 10) with a thickness of 1.5 mm and has a meander line with width of 2.85 cm. The second, Figure 11, uses Teflon as

the dielectric ($\epsilon = 2.1$) with a thickness of 0.8 mm and has a meander line width of 5.0 cm. The LTCC case was driven first with a constant voltage, then with a 1.0 GHz sinusoidally varying voltage. The Teflon configuration was driven only with the 1.0 GHz voltage. Current monitors were placed on several legs of the meander line. Figure 12 and Figure 13 show the output from selected current monitors for the steady-state drive. The boundary condition used a voltage of 600 V. The boundary condition consists of a cylindrical opening in a conducting surface into which the end of the meander line is inserted. The end of the meander line is cylindrical; this mates onto the ribbon shape used for most of the line. The radius of this cylindrical part of the meander line is 0.1 cm. The radius of the cylindrical opening is 0.2 cm. Looking at this geometry as a transmission line, it would present an impedance of $Z = (60 \Omega) \ln(r_{\text{out}}/r_{\text{in}}) = (60 \Omega) \ln(2) = 41.6 \Omega$. With a voltage of 600 V applied to the boundary, one would expect a steady state current of $600 \text{ V} / 41.6 \Omega = 14.43 \text{ A}$ to be produced in the meander line. Figure 13 indicates a steady-state current of 15.87 A. Given that the spatial resolution used here is somewhat coarse relative to the size of the boundary condition radii (0.1 and 0.2 cm; $\Delta x = 0.0195 \text{ cm}$), the difference between the observed steady-state current and that expected on the basis of the coaxial TEM impedance is neither surprising nor unacceptable. The relative error between the observed steady-state current and the expected steady-state current is 10.0%.

In Figure 13, the time at which each current monitor shows its initial response to the drive can be used to measure the propagation speed of the wave along the meander line. For example, the time delay between the Leg 30 response and the Leg 40 response is approximately 2.3 ns (looking at the time the current reaches 10 A on each trace). The dielectric has relative permittivity of $\epsilon_r = 7.8$; the distance travelled by a light wave through such a medium in 2.3 ns would be $s = (2.3 \text{ ns})(3 \times 10^{10} \text{ cm/s}) / (7.8)^{1/2} = 24.70 \text{ cm}$. Given that 10 legs of the meander line separate the Leg 30 current monitor from the Leg 40 current monitor, a wave has to travel roughly 28.5 cm to get from the Leg 30 station to the Leg 40 station. The agreement between this and the simple estimate of Leg 30/Leg 40 delay is not bad.

Figure 14 shows the vertical component of magnetic field in the interaction region for the case of the steady drive voltage. The magnetic field alternates in sign between each pair of meander line legs as it must since the steady current alternately flows into and out of the plane of the plot. The plot shows that the amplitude of the field variation is relatively flat throughout most of the interaction region. Figure 15 shows the current on the input and output legs of the meander line for the case of the 1 GHz sinusoidal drive. Notice that the amplitude of the current is different from the current driven by the steady drive; for the sinusoidal drive, the current amplitude is 15.004 A while for the steady drive, the current attained a steady value of 15.87 A. Figure 16 shows the y-component of magnetic field produced by the harmonically driven line. Correlating the strength of the x-component of electric field to the voltage applied at the boundary is valuable. For a 1 GHz, 600 V drive, the electric field amplitude at a height of 2 mm above the sole plate is 400 V/cm; thus, at this height above the sole plate for the case of the LTCC dielectric, a wave amplitude of 0.667 V/cm is produced per volt applied to the boundary. That can be translated to input power using the observed current amplitude of 15.004 A and drive of

600 V to deduce an actual input impedance of 39.99Ω . The sinusoidal drive at 600 V thus should correspond to an RF power input of $V^2/2Z = 4501 \text{ W}$. Thus, the calibration between wave amplitude at 2 mm above the sole plate and input RF power on the meander line is 0.0889 V/cm per watt of input RF power. The calibration for the Teflon dielectric is one watt of RF input power produces a wave amplitude of 0.142 V/cm at a height of 2 mm above the sole plate.

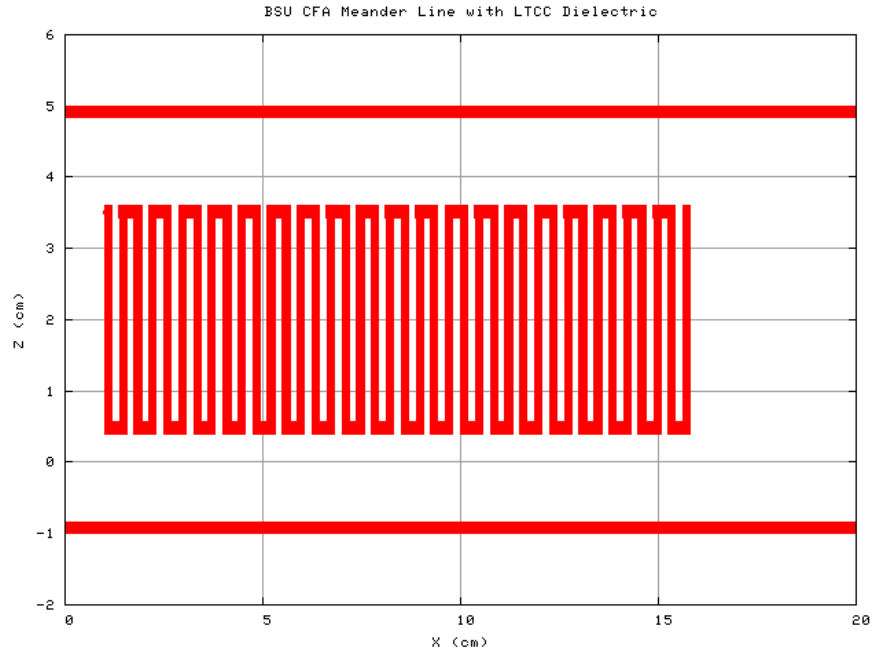


Figure 10: Meander line geometry for the CFA with LTCC dielectric (2.85 cm meander line width, 1.5 mm dielectric thickness)

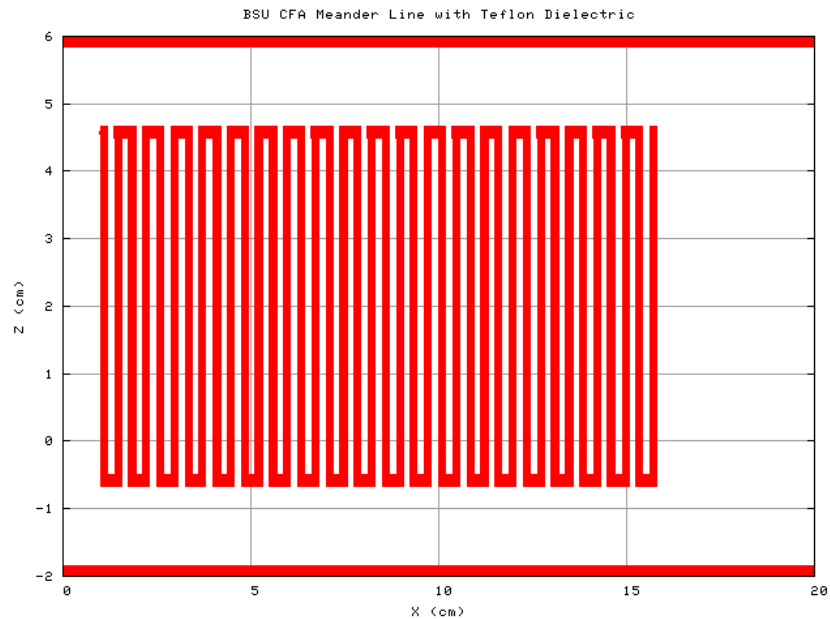


Figure 11: Meander line geometry for the CFA with teflon dielectric (5.0 cm meander line width, 0.8 mm dielectric thickness)

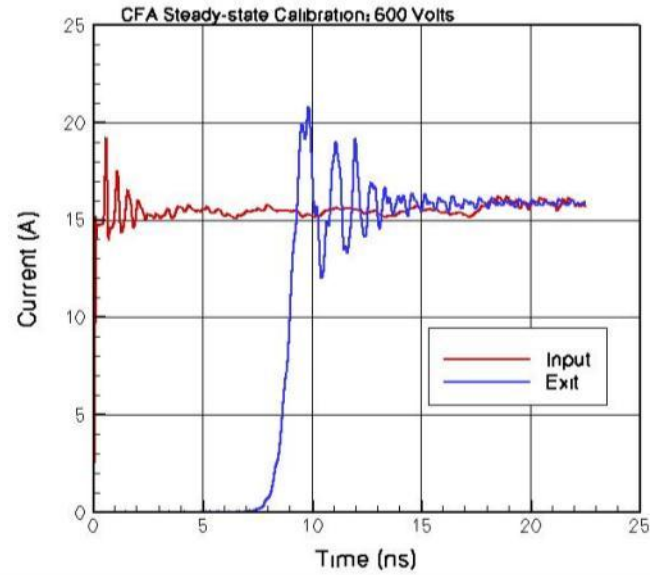


Figure 12: Current monitored at input and output legs of CFA meander line (LTCC dielectric) under steady drive conditions (600 V).

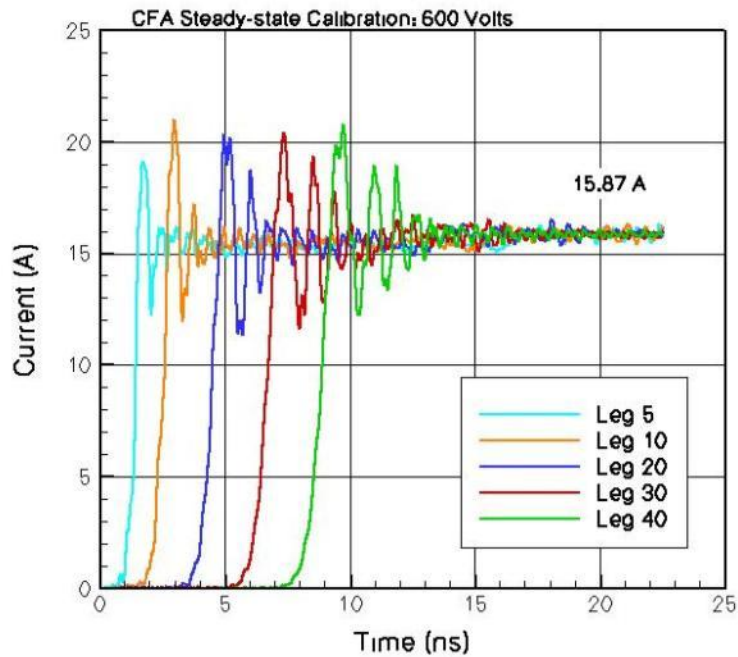


Figure 13: Current monitored at selected legs of CFA meander line (LTCC dielectric) under steady drive conditions (600 V).

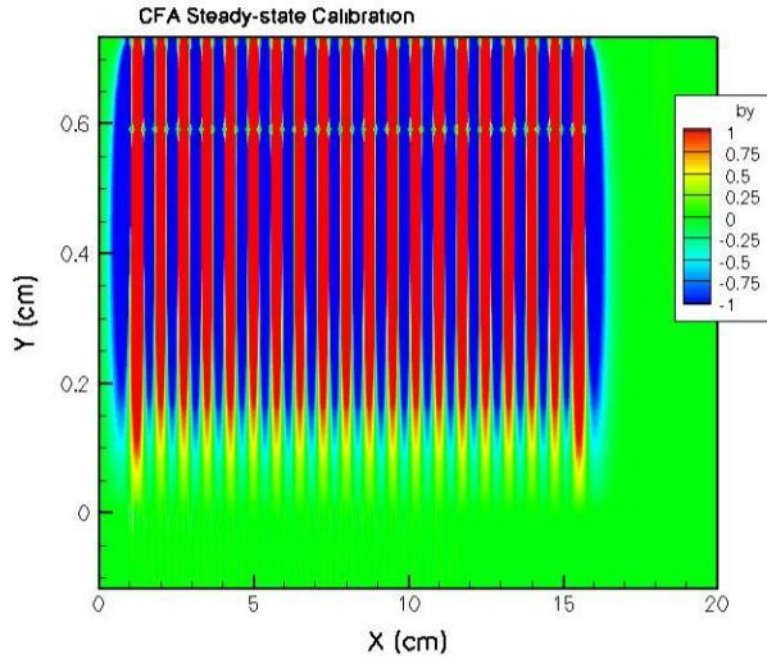


Figure 14: Vertical component of magnetic field between meander line and sole-plate produced by steady meander line drive. Axial field variation correlates precisely with meander line leg-to-leg separation.

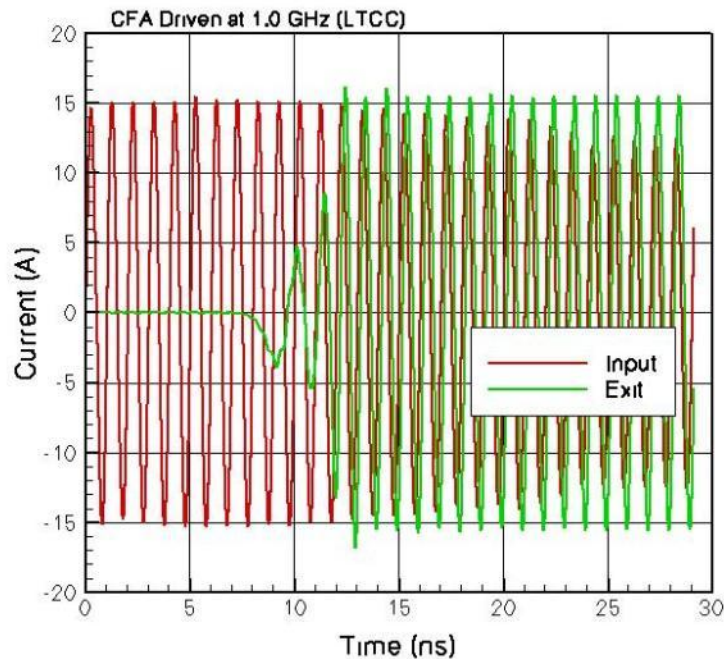


Figure 15: Current monitored at input and output legs of CFA (LTCC dielectric) under 1 GHz drive conditions (600 V).

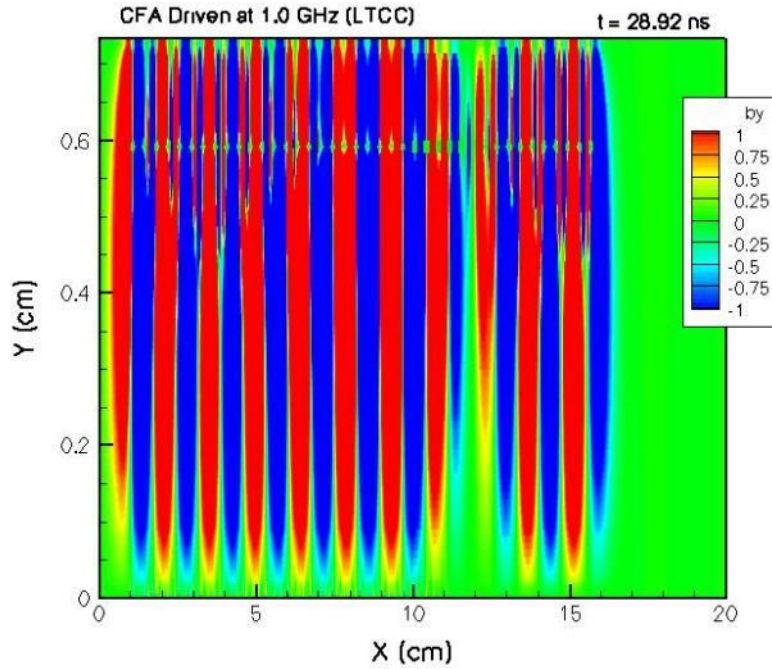


Figure 16: Vertical component of magnetic field between sole plate and meander line produced by 1 GHz, 600 V drive (LTCC dielectric). Observe difference in axial variation between this and that produced in steady-state drive conditions.

As a further test of the model developed to represent the meander line, calculations were conducted using different values for the drive frequency. Figure 17, Figure 18, and Figure 19 show the x-component of electric field along the chord $y = 0.2$ cm along the length of the device for drive frequencies of 875, 1125, and 1000 MHz, respectively. The plots show that for drive frequencies not close to the design frequency of 1000 MHz, the line fails to produce a clean, sinusoidal travelling wave in the interaction region, while for the design frequency of 1000 MHz, the field close to the sole plate is dominated by a sinusoidal travelling wave.

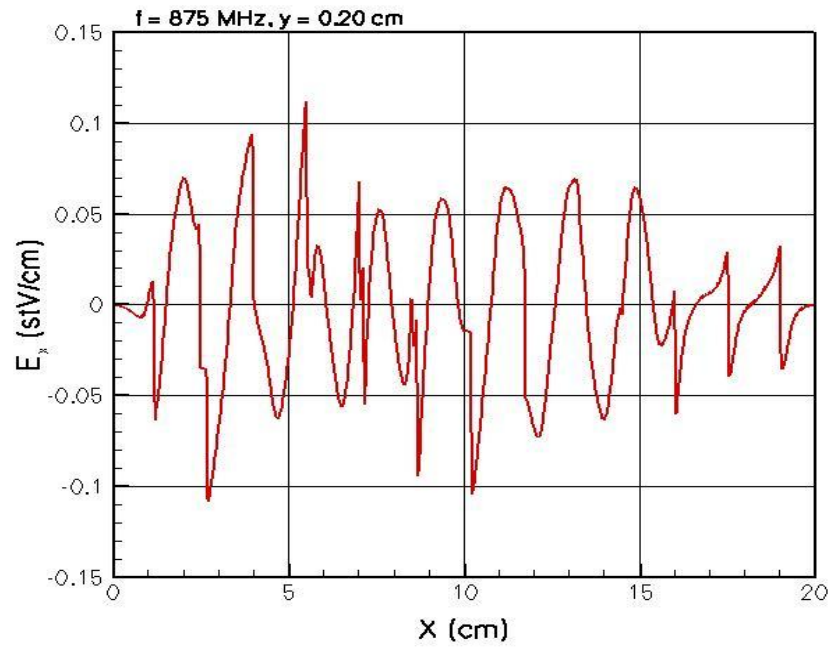


Figure 17: x-component of electric field produced by meander line at 875 MHz along a chord 0.2 cm above the sole plate

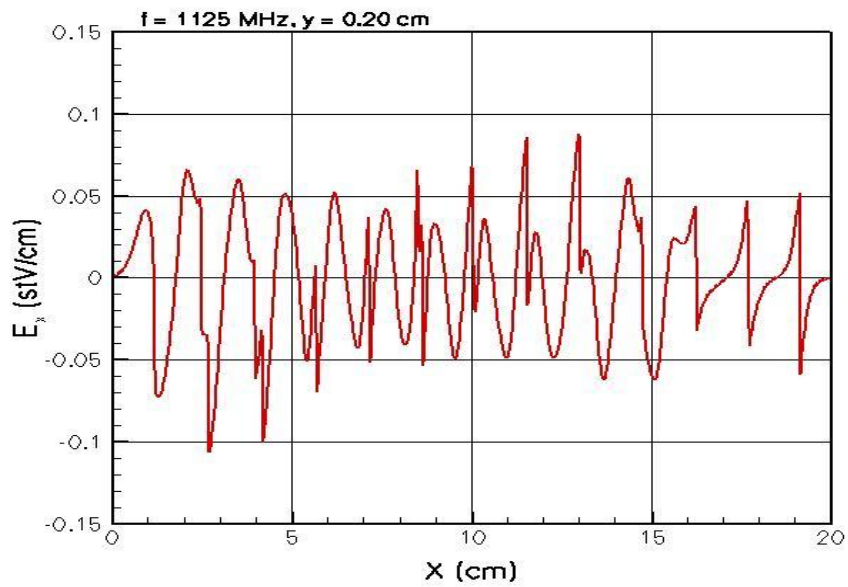


Figure 18: x-component of electric field produced by meander line at 1125 MHz along a chord 0.2 cm above the sole plate

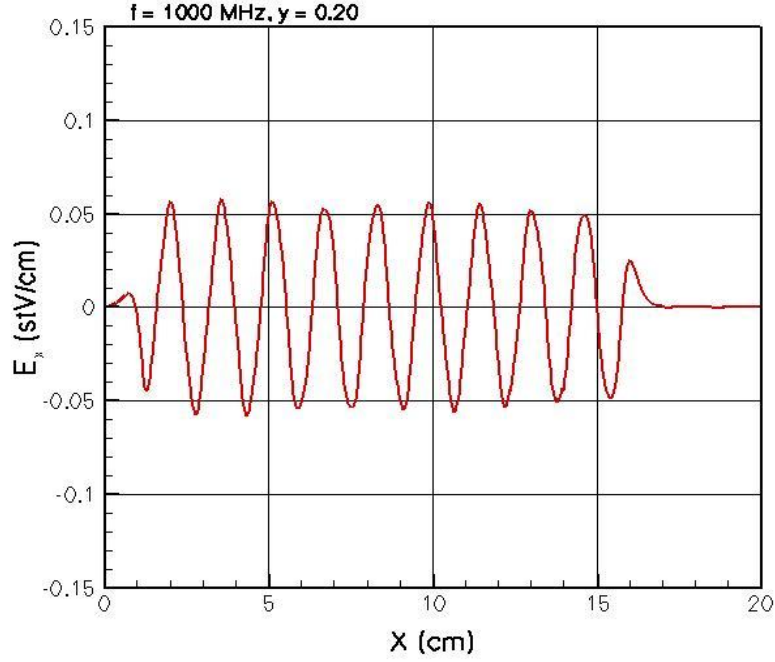


Figure 19: x-component of electric field produced by meander line at 1000 MHz along a chord 0.2 cm above the sole plate

With the essential operational characteristics of the ICEPIC model checked, attention turned to the behavior of particles. A first step was to confirm that ICEPIC faithfully depicted the basic $E \times B$ motion of electrons in the combined applied vertical (y-component) electric field and into-the-plane (z-component) magnetic field. This may not seem an important step for in applying a relatively mature code such as ICEPIC, but the user has experienced multiple occasions in which code modifications made by others had the unintended consequence of negatively affecting the particle trajectory calculator (trust, but verify). The equations of motion describing an electron at rest, accelerated away from the sole plate by the spatially uniform applied electric field and influenced by the spatially uniform applied magnetic field were solved and compared to ICEPIC trajectories of a test particles (particles whose charge was chosen to be sufficiently small as to have an infinitesimal effect on the ambient electric and magnetic fields). The solution to the equations of motion is:

$$\begin{aligned}
 x(t) &= \frac{1}{2} \frac{a}{\sqrt{b}} \left[t - \frac{1}{\sqrt{b}} \sin(t\sqrt{b}) \right] \\
 y(t) &= \frac{1}{2} \frac{a}{b} \left[1 - \cos(t\sqrt{b}) \right] \\
 a &= 2 \frac{e}{m} |E_0|, \quad b = \left(\frac{eB_0}{mc} \right)^2
 \end{aligned} \tag{0.1}$$

This describes a trajectory that moves steadily in the positive x-direction while describing a periodic excursion away from the sole plate and subsequent return. The height achieved by the trajectory above the sole plate and the distance between points of successive returns to the sole plate are related. Inspection of the solution of the equations of motion indicates that the turning point height (H) and the hop distance (L) are

$$H = \frac{a}{b} = \frac{2 \frac{e}{m} |E_0|}{\left(\frac{eB_0}{mc} \right)^2} \quad (0.2)$$

$$L = \pi H$$

The trajectories generated by two test particles launched from closely neighboring points are shown in Figure 20. The trajectory vertical travel is normalized by the height H and the horizontal travel is normalized by the hop distance $L = \pi H$. The ICEPIC results are in very good agreement with the solution of the equations of motion.

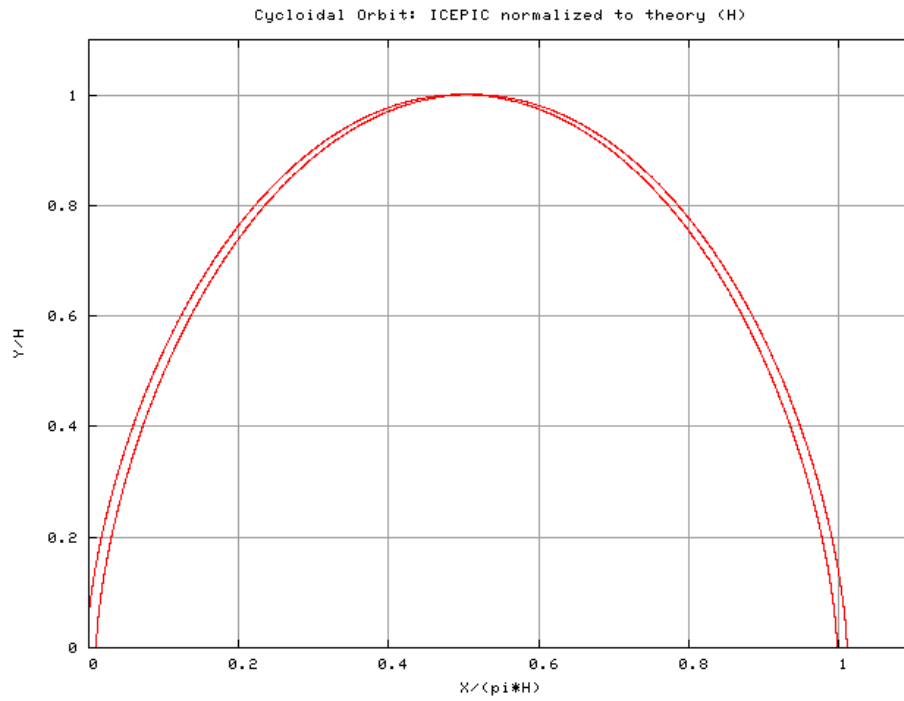


Figure 20: Cycloidal trajectories of test particles in crossed uniform applied electric and magnetic fields as calculated by ICEPIC and normalized to theoretical values of height H and hop distance πH

With the accuracy of the ICEPIC cycloidal trajectory calculation confirmed, efforts turned to exploring the interaction between electrons and the electromagnetic waves produced by the meander line. Several different approaches were used for launching the electrons, but it soon became clear that the priority was to settle on an acceptable launch model and focus on exploring the wave/particle interaction. A simple launch model in which electrons were injected from a pedestal raised very slightly above the level of the sole plate was adopted. Calculations were conducted in which the injected electron current was varied from one calculation to the next while the meander line amplitude was not varied. Figure 21 depicts one such calculation at a time such that steady-state operation has been attained. Other calculation series were conducted in which the electron launch current was maintained at a steady value while the amplitude of meander line drive was varied from one calculation to the next. These calculations failed to produce an increase in the meander line current, which was considered the sign of an interaction that transferred energy from the electrons to the electromagnetic wave and subsequently into the meander line.

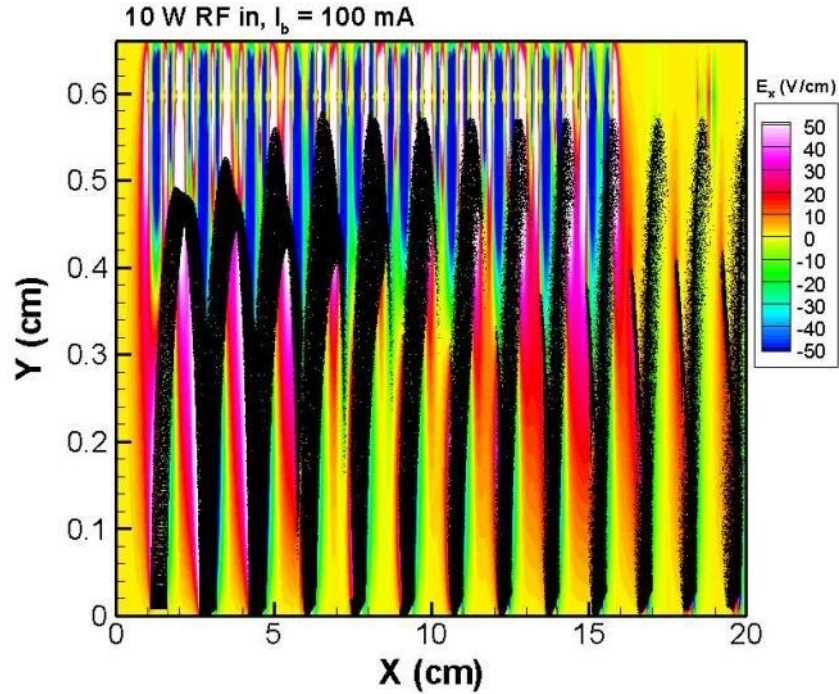


Figure 21: Full CFA calculation with 100 mA electron beam injected into field pattern produced by the meander line driven at 1.0 GHz with input power of 10 W. Particle positions and x-component of electric field are shown during steady-state phase of the calculation.

A reduced physics model was developed to allow rapid exploration of the parameter space characterizing the CFA. The ICEPIC calculations, with millions of macroparticles representing the electrons and tens of millions of cells discretizing the simulation domain,

took several days apiece to produce useful results. The reduced physics model consisted of test-particles moving in a specified set of electromagnetic fields. The electromagnetic fields consisted of the applied electric and magnetic fields and a harmonic traveling wave. With the fields completely specified in this manner, the reduced physics code spent most of its time computing motion of a few hundred test particles. This provides a run-time of a minute or less. This allows a wide range of parameter space to be explored. The reduced physics code was configured so that the test-particles moved only in the x-direction and were subject to a harmonic wave with x-component of electric field. The test particles all were injected with the same energy. Individual test particles gained or lost energy, depending on when relative to the phase of the harmonic wave they entered the simulation. The energies of the test particles at the downstream end of the simulation domain were averaged and compared to the initial energy. The results of such calculations in which the beam speed varied around the $1.5e9$ cm/s phase speed of the harmonic wave are shown in Figure 22. The results show that a beam with average speed greater than the wave phase speed will tend to give up energy on the average.

These and similar reduced physics model results were intended to guide further ICEPIC calculations. In order to make the connection between ICEPIC and the reduced physics model prediction, detailed measurements of the wave phase speed in ICEPIC calculations were initiated. This revealed an aspect of the fields produced by the meander line that had not been fully appreciated up to this point. Figure 23 shows the vertical (y) component of electric field along chords at various heights above the sole plate. The assumption of a sinusoidal travelling wave appears to be violated grossly for heights above the sole plane in excess of 0.36 cm. Were these higher order waves to be travelling at the same phase speed as the desired fundamental mode, they would likely be of little consequence. However, animations of these results (which unfortunately cannot be reproduced within this static document) reveal that the higher order modes travel backwards. The top half of the electrons' cycloidal trajectory thus extends into a region that is occupied by short wavelength, backward moving waves with amplitude comparable to that of the desired fundamental mode. Figure 24 shows a Fast Fourier Transform of the electric field vs. x data at a height of 0.5 cm above the sole plate, quantifying more accurately the relative magnitudes of the fundamental and higher order modes. Subjecting the electrons to this environment for over roughly half of their trajectory violates the basic assumption of interaction with the simple fundamental travelling wave and is not likely to be beneficial to the desired interaction.

The desired course of action at this point would be to develop a theoretical description of the full set of wave modes being created by the meander line, vet the theory by comparison to ICEPIC calculations, look for corroboration of theoretical and simulation predictions in detailed laboratory measurements while simultaneously developing a theoretical and simulation-based description of wave-particle interaction in the actual electromagnetic environment. The meander line, in this desired course of action, would then be redesigned following guidance developed from the theoretical and experimental assessment of the higher order modes, and new experiments using the redesigned meander line would be mounted. Unfortunately, the scope of this effort did not allow such an ambitious course of action. Rather, a simple redesign of the meander line was considered within ICEPIC calculations.

The simple redesign consisted of increasing the distance between the sole plate and the meander line by 0.3 cm. What this does is simply drop the electron trajectory down to the point where the entire vertical extent of the trajectory remains within the fundamental mode. This takes advantage of the observation that the amplitude of the higher order modes drop off with distance from the meander line much more rapidly than does that of the fundamental mode. This might result in a drop in efficiency as the amplitude of the fundamental mode does decrease, thus decreasing the interaction between waves and particles, but more important than efficiency is demonstration of basic operation without regard to efficiency.

With the device modified by dropping the sole plate down by 0.3 cm, a cold calculation was performed to assess the importance of the higher order modes at what would be the new location of the top of the cycloidal trajectories. Figure 25 shows the Fourier transform of the electric field vs. x data. The amplitude of the higher order mode is now approximately 26 dB below that of the fundamental mode whereas in the original design, the higher order mode was only about 3 dB below that of the fundamental. With the redesign, the fundamental mode dominates electron trajectories over the entire span of vertical travel.

Figure 26 shows the total energy of particles in two different calculation – one in which the meander line was present, but not driven, and a second in which it was driven. The calculation with the passive meander line shows a slight variation in electron total energy (kinetic energy plus the potential energy associated with the spatially uniform applied vertical electric field) due to the beam's own space charge. With the meander line driven, the total average particle energy undergoes a steady decrease as the beam travels along the device. Figure 27 shows another calculation, this one with a 100 mA beam and the meander line driven with 280 W of input RF power. The average particle losses approximately 6.5×10^{-10} ergs. With the beam current of 100 mA, this represents a power transfer out the beam of 40.6 W. This indicates interaction of the desired sort, but clearly is need of some optimization.

Future work is hoped to build on progress made and summarized here. Use of the reduced physics model will help guide ICEPIC calculations toward better choices of drive power and beam current. Theoretical analysis of the meander line and interaction of electrons with the higher order modes will guide possible redesign of the meander line.

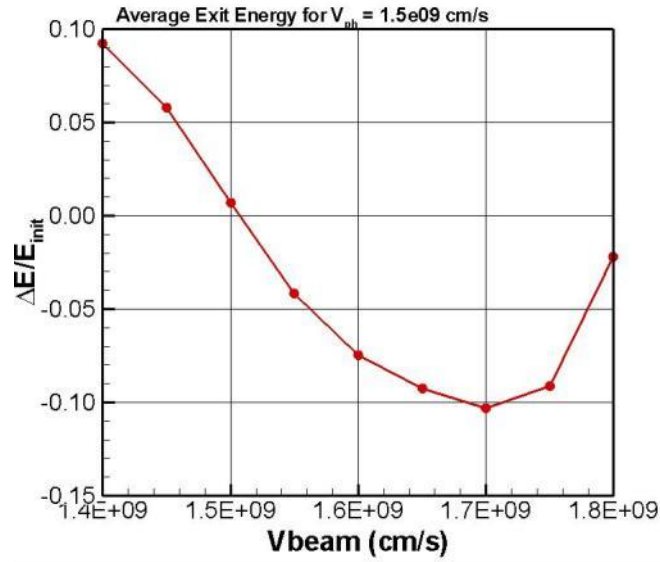


Figure 22: Reduced physics model for one-dimensional particle motion with harmonic wave with $V_{ph} = 1.5e09$

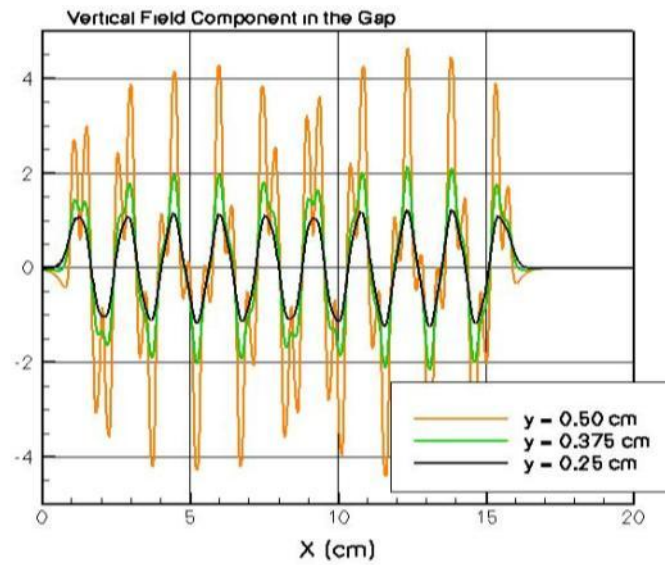


Figure 23: y-component of electric field along chords at various heights above the sole plate

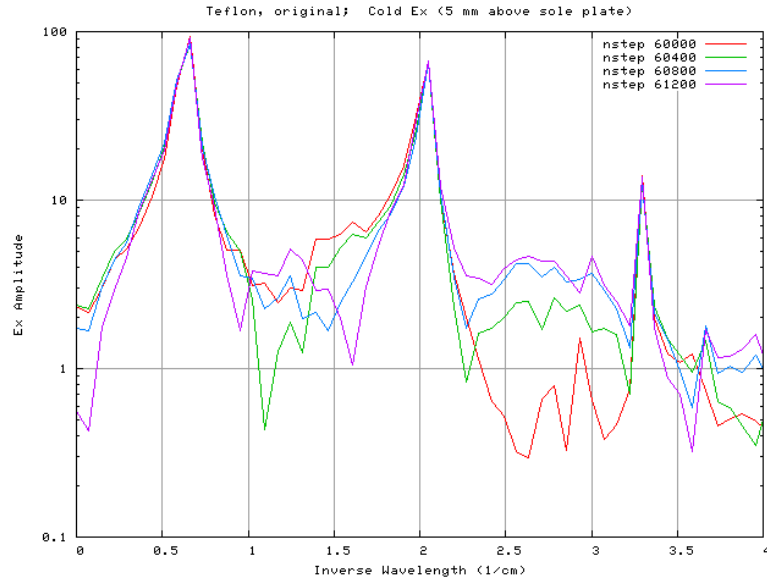


Figure 24: Fourier transform of x-component of electric field along a chord 0.5 cm above the sole plate.

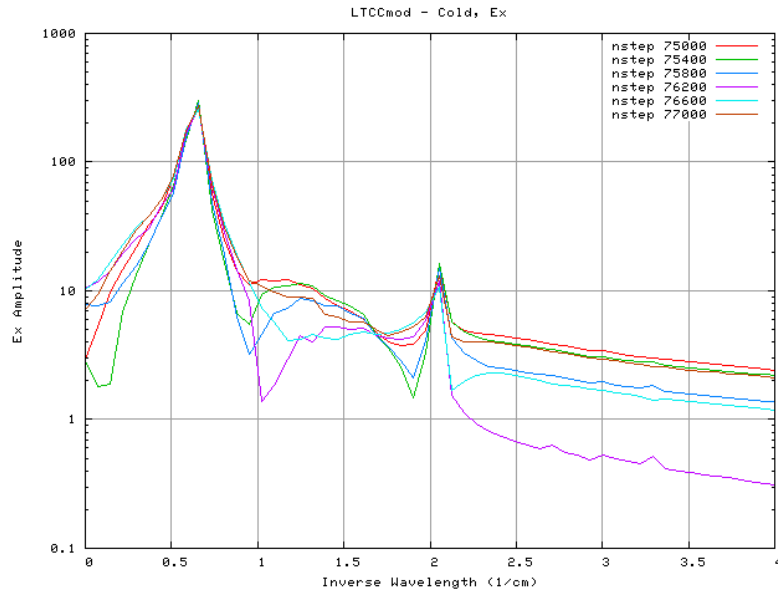


Figure 25: Fourier transform of x-component of electric field along a chord 0.5 cm above the sole plate with distance between sole plate and meander line increased from original design by 0.3 cm.

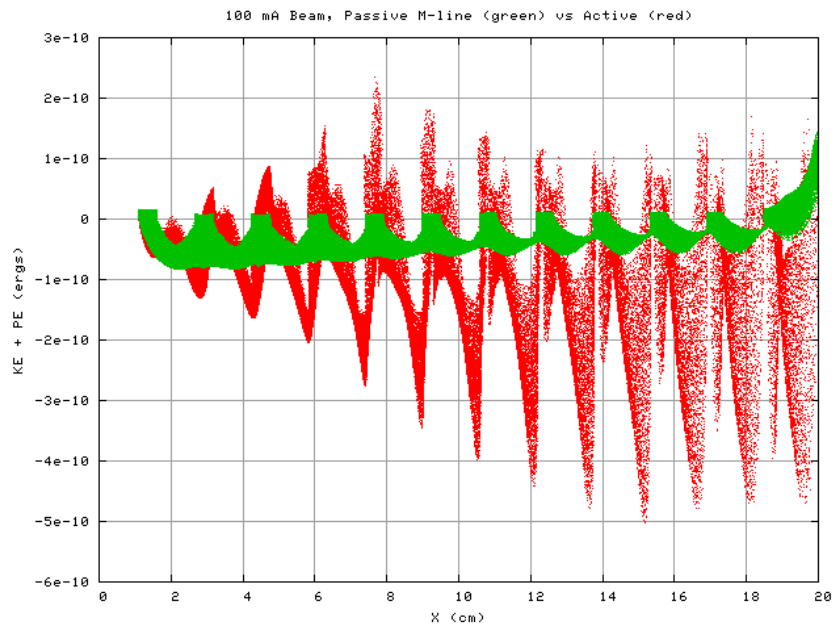


Figure 26: Total (kinetic plus potential) energy of a 100 mA beam of electrons in modified CFA with an undriven meander line (green) and a line driven at 1.0 GHz (red)

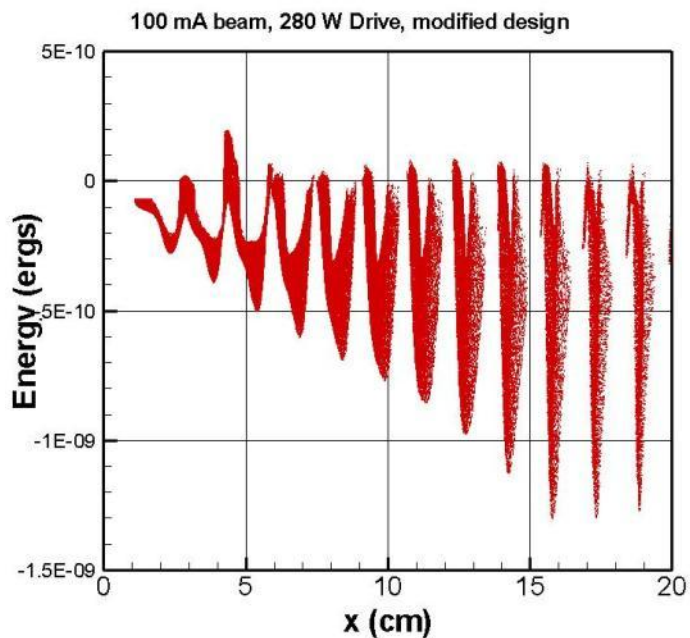


Figure 27: Modified CFA design with 100 mA beam and meander line driven with 280 W showing secular decrease in total particle energy

VI. Control Electronics

A. Basic Control System

We have acquired National Instrument control and acquisition hardware for the laboratory setup. The setup consists of NI PXI-1033 Chassis with PXI 6541, PXI 6259, and PXI GPIB control and acquisition boards. Figure 28 shows the current setup. The setup is interfaced to the control through PCI-Express interface. This interface has the ability to transfer large amount of data quickly and efficiently. The GPIB interface is used to control the frequency generator and to capture data from a spectrum analyzer. The software control has been implemented with Labview. The high voltage hardware is floated using a Glassman 5 kV, 0.4 A power supply. This supply provides the electron beam current. The sole electrode and field emission cathode voltages are provided by three Dc to DC converters. The voltage control and current measurements are transferred through a series of opto-couplers. Figure 28 (right side) shows the high voltage isolation box with the DC to DC converters, AC to DC power supplies, isolation transformer, resistor box, and opto-couplers. Although this system allowed control of the overall CFA system, the field emitter arrays represented a different set of issues.

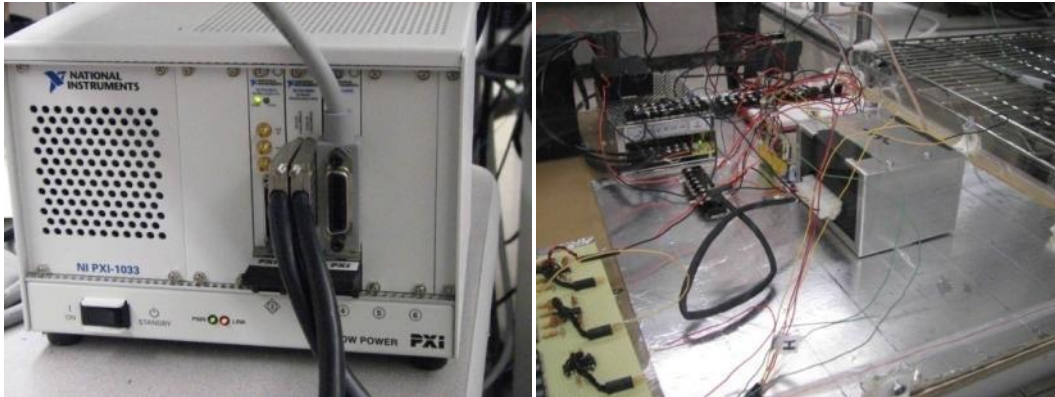


Figure 28. The left picture shows the National Instruments PXI 1033 Chassis with PXI 6541, PXI 6259, and PXI GPIB control and acquisition boards. The right picture shows the interface circuitry in a high voltage isolation box.

B. Field Emission Controllers

The cathodes are made up of arrays of field emitters. As described earlier, three types of emitters were used: Stellar Lateral Emitters, Motorola Display Spindt Emitters, and PixTech Display Spindt Emitters. These arrays operate over a range of voltages (50 to 500 V) and varying degrees of leakage currents. The control system was intended to drive eight arrays, or elements, of emitters with the total injected beam current regulated for each element. Since the current flowing through the emitter includes injected current, current going back to the emitter gate, and resistive leakage current, the current control requires that the gate current be subtracted from the emitter current in real time. To that end, the Field Emitter Control and Measurement System (FECMES) was developed.

The FECMES provides the capability to control the current generated by a set of field emitter devices and to measure the current leakage to the gate circuits. Experimental tests using the CFA structure require knowledge of the amount of current entering the channel. Unfortunately the Field Emitter Arrays (FEA) currently available have appreciable amounts of leakage current, diverting a portion of the current entering the emitter away from the channel. A measurement system is required in order to measure this leakage current. The gate current will be the sum of these leakage current values, while the remaining current represents current into the channel. The gate structures are biased to a high voltage, in the 100V to 500V range. This high bias voltage makes current measurement more difficult. At first it might seem that a low-side current sense would work. While this would be possible with a single gate, it would be expensive with an array of gates. A low-side current sense would require multiple high-voltage power supplies. This technique is limited by the cost constraints of such supplies.

The FECMES system was designed to resolve the issues presented by these high voltages and to provide a control system located at the local ground potential. The control system is then connected to the main host computer using a serial link and high-voltage optical isolators. The host computer uses Lab View for a control environment.

The idea behind using the FECMES system is to have one centralized location that can monitor and control the experiments performed in the vacuum chamber for the CFA project. Labview gives us the ability to interface with our controller board via a serial connection to monitor our system, while at the same time communicate with our DAQ devices. Using the FECMES system we have the ability to perform automated sweep tests on our equipment. The system consists of a controller board, current board, and emitter board as shown in Fig. 29.

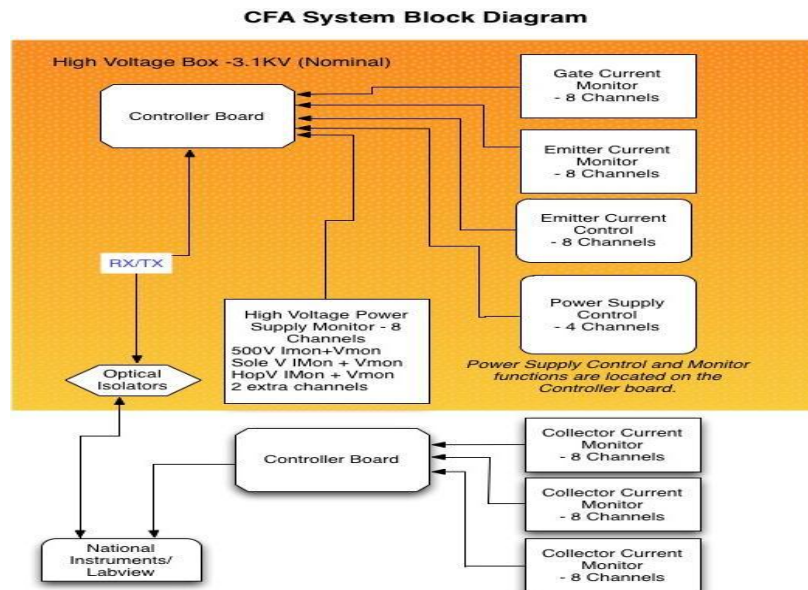


Figure 29. Diagram for FECMES system

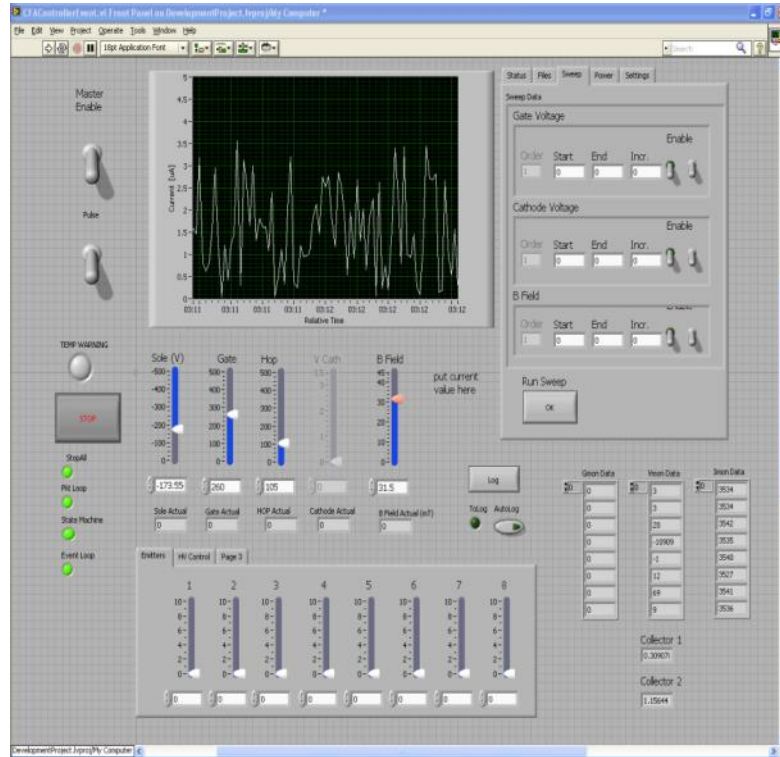


Figure 30. Labview Screenshot

The goal for the software implemented in the Field Emitter Control and Measurement System was to utilize modular coding structures which could be easily added to or modified during future, possibly unforeseen, tests of the CFA project. This concept was utilized during the design stage through the use of a class based coding style in Labview, allowing for future additions and relatively simpler modifications. Base classes were used to create objects for each piece of equipment that contained the correct information to control that piece of equipment, such as a voltage change or a current read. Because each class is then an implementation of the base class we could create a reference to the object in question and place it into an array with other objects. This array of pointers to objects can then be passed to any Virtual Instrument (VI) that has a need to control the equipment. In addition, a coding style known as the producer and consumer model was implemented wherein one main event loop handles all registered events. These events include user controls, timers, receiving of data packets from the controller board, and any other functionality deemed necessary. The benefit here is to have multiple loops running at the same time keeping CPU usage relatively low. A picture of our current top level VI design in Labview can be seen in Fig. 30.

The controller board contains a microprocessor and analog circuitry needed to interface to the High Voltage (HV) power supplies. The microprocessor is an Atmel ATxmega192A3 which includes dedicated SPI interfaces and built in 12bit ADC. The ADC is used for measuring the voltage and current monitoring outputs from the HV supplies.

The controller board, shown in Fig. 31, provides the following capabilities.

1. Control and Measurement for four High Voltage (HV) power supplies.
2. Interfaces to two Current Monitor boards, one for the gate circuits and one for the emitters.
3. Interface to an Emitter Driver board.
4. Dual 3.3V level RS-232 interfaces to the host computer.

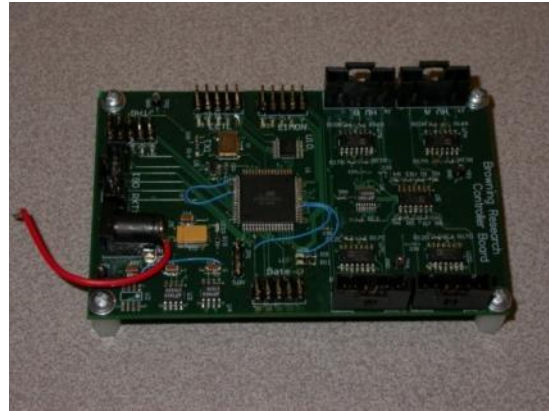


Figure 31. Controller Board

The controller board firmware is written in C++. The firmware uses a pair of serial connections for communication and data transfer. The primary connection is a command channel. The firmware uses a command/response mechanism to provide feedback to the controller. All commands are acknowledged with an Ok or Fail response, along with response data for read commands. The data channel uses a broadcast only mechanism. The firmware is configured to perform measurements at periodic rates. The measurement results are broadcast back to the controller without acknowledgement. This broadcast mechanism eliminates the need for the controller to poll for data, and insures that the controller receives updated measurement information as soon as it is available. The firmware development environment uses any text editor for code development. AVR Studio is used to compile the code into a suitable hex file and the AVR JTAG ICE MkII is used for processor configuration and debug.

The current monitor board shown in Fig. 32 is used to monitor the current into or out of the gate circuits. The challenge with this measurement is that the gate circuits are biased at a high voltage of as much as 500V. The current monitor circuit uses a digital coupler device with an isolated power circuit. The Analog ADuM5401 device is rated for 2500V spikes. In the current monitor circuit the need is to stand off 500V continuous. From discussions with Analog engineers some small print in the specification shows that the devices can work for long periods of time (years) with a voltage >500V making them well suited for this application. The devices would not work if higher voltage differences were required.

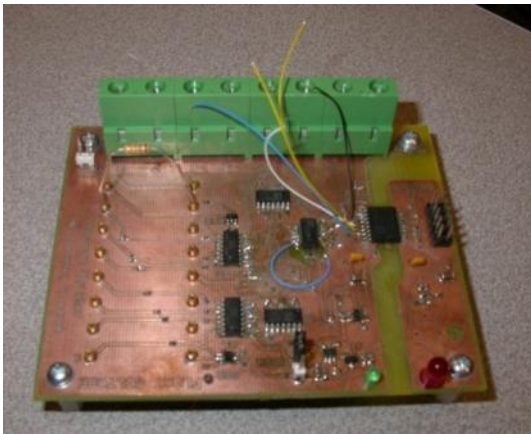


Figure 32. Current Monitor

A low voltage side and high voltage side were achieved in the circuit by utilizing the ADuM5401. The iCoupler circuit in the ADuM5401 provides an isolated voltage, V_{ISO} , for use on the high-voltage side. In this case, V_{ISO} was used in the current monitor to provide power to a 16 bit-8 channel ADC, operational amplifiers, and voltage references.

This high voltage floating measurement circuit can then measure the gate current directly floating with the gate voltage. The iCoupler device allows the control signals for the ADC to pass through the high voltage offset to the low voltage controller.

Emitter Driver Board

The emitter driver board is used to control the current into the emitters. The key element of the emitter driver board is a high voltage FET which is capable of holding off $>500\text{V}$. The emitter driver uses an operational amplifier and a sense resistor to set a desired current into the emitter. When this emitter current is set to zero, the emitter will be off, causing the source of the FET to float to the full Gate voltage level (up to 500V), and the drain of the FET to drop to a much lower voltage. Figure 33 shows the FET circuit, with the I_{sink} connection. The I_{sink} connects to a resistor then to ground, where the resistor is used by the current monitor board to sense the emitter current. The voltage across this sense resistor is proportional to the emitter current. The inverting input to the operational amplifier is centered between the emitter current sensor resistor and a low voltage reference voltage. V_{reflv} is set to 0.5V . This voltage offset allows the control input on the non-inverting input to drive the operational amplifier completely off. Without this offset the normal input voltage offsets of the operational amplifier might result in a very small current flowing in the FET even with V_{in} set to zero. Zero is rarely 0.0V in a real circuit, and input voltage offsets on typical operational amplifiers can be several mV . The V_{reflv} offset means that a V_{in} voltage less than about 0.25V will force the amplifier output to its minimum output voltage level, near 0V , and turn off the FET. With the FET off, the only current flowing in the emitter will be based on FET leakage currents.

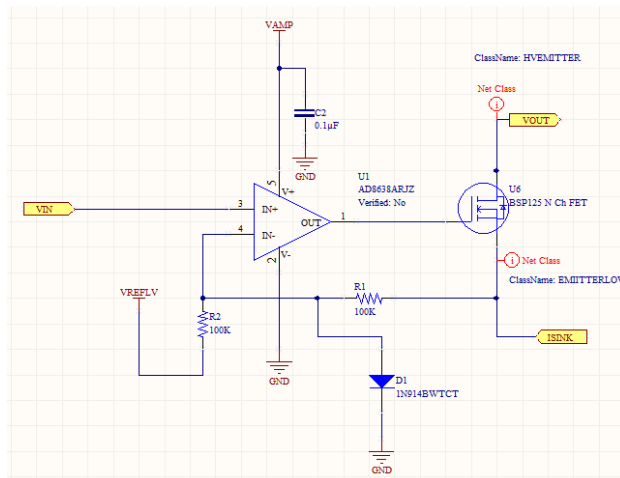


Figure 33. FET circuit

control accuracy will be limited by the voltage input offsets of the operational amplifier and the precision of the emitter sense resistor.

The emitter driver board has the sockets to use local emitter sense resistors. In this configuration it will not be possible to measure the emitter current directly, but the current can be calculated based on the setting voltage. If the emitter circuitry is working as expected, this setup does not represent an issue. If the setup does not generate the current expected, or there are opens in the circuit, then the expected current will not

The ideal FET for this circuit must withstand the high voltages between source and drain and have a minimum leakage current. Any leakage of the FET will cause current into the channel with the device off. Leakage values of $1\mu\text{A}$ or less are desired.

The emitter driver board includes a 16bit octal output 0-5V DAC onboard. This DAC generates the V_{in} voltage shown above. There is an onboard 5V reference for the DAC to insure voltage accuracy. The current

match the actual current.

Since the emitter connections may see voltages as high as 500V, a high voltage screw terminal connector was used. This connector is rated at 500V for safety. The ground and power planes on the PC Board were pulled back from these pins in order to avoid potential arcing on the board. Arcs in the chamber could potentially cause high voltage spikes on the drain side of the FET. To help avoid circuit problems a transient suppression diode was placed between the 100 k Ω resistors.

VII. Hop Funnel Physics and Simulation

The hop funnel design is based on the simulation efforts using the Lorentz code. In addition, the hopping properties of LTCC are important. Therefore, a significant experimental and simulation effort of this program looked at the electron hopping of the LTCC funnels and compared these results to the predictions of the Lorentz2E simulation. The simulation was modified by the vendor over time to take into account issues that were discovered when performing the simulations of the hop funnels. Since Lorentz2E is a two-dimensional code, a true funnel rather than slits were used for many of the experiments. The experimental pictorial is shown in Fig. 35. Here an LTCC hop funnel (hole) is used with Motorola or PixTech field emitters. The hop funnel is placed over the emitter, and an anode is placed above the hop funnel to measure the emitted current out of the funnel. In this figure a discriminator grid and ground grid are shown for experiments when the electron energy distribution was measured. The I-V characteristics of the funnels were often noisy and showed a significant hysteresis. The emission current noise is related to large leakage currents in the cathodes. The normal current stabilizing circuitry would not work, but the new hardware (described above) should help keep the current constant for future work. Nonetheless, I-V curves were measured along with electron energy distributions. These results and the simulation results are described in great detail in the paper by Lester, et. al.¹

For brevity, the details of that research are not included here, but more recent results are presented. In the simulations, the effect of the hop electrode voltage on emission can be readily observed. When the hop voltage is too low, electrons are turned back by the charge on the hop funnel wall. When the voltage is large enough, the electrons hop out due to secondary electron emission. These conditions have been simulated in order to generate I-V curves.

Shown in Fig. 36 is a simulation of the electron rays from the field emitter. These rays, representing some fraction of the total current, strike the hop funnel wall and generate secondaries. Since the hop voltage is only 170 V, the electric field is not large enough and the secondary yield is too low for unity gain. Some primary electrons and a few secondaries escape. The wall charge becomes negative and turns back the bulk of the electron rays. If the hop electrode voltage is large enough, the electrons will hop until

¹ C. Lester, J. Browning, and L. Matthews, "Electron Hop Funnel Measurements and Comparison with Lorentz2E," IEEE Trans. on Plasma Sci., Vol 39, No. 1, January (2001)

they escape. At a high enough voltage, the current out is equal to the current in, or the device has unity gain. This mechanism greatly averages the current distribution in the hop funnel and improves the emission uniformity. Simulations of this are shown in Fig. 37 where the secondary electrons from the hop wall escape. Using this technique, the I-V characteristics can be simulated and compared with the experimental results as shown in Fig. 38. Note that the simulation allows input of the maximum secondary emission yield (δ_e), the energy at which the maximum yield occurs (W_m) and the average secondary energy (5 eV was chosen). Since the secondary yield values for LTCC are not known, values were chosen to fit the data. It was shown that the key to fit the IV curve is the first crossover of the secondary yield (where it goes through unity). Any values of δ_e and W_m that gave 70 eV would fit the IV curve because the simple model used in the simulation had identical values of yield below 70 eV. Therefore, the simulation could not be used to determine the secondary parameters. A new approach was needed.

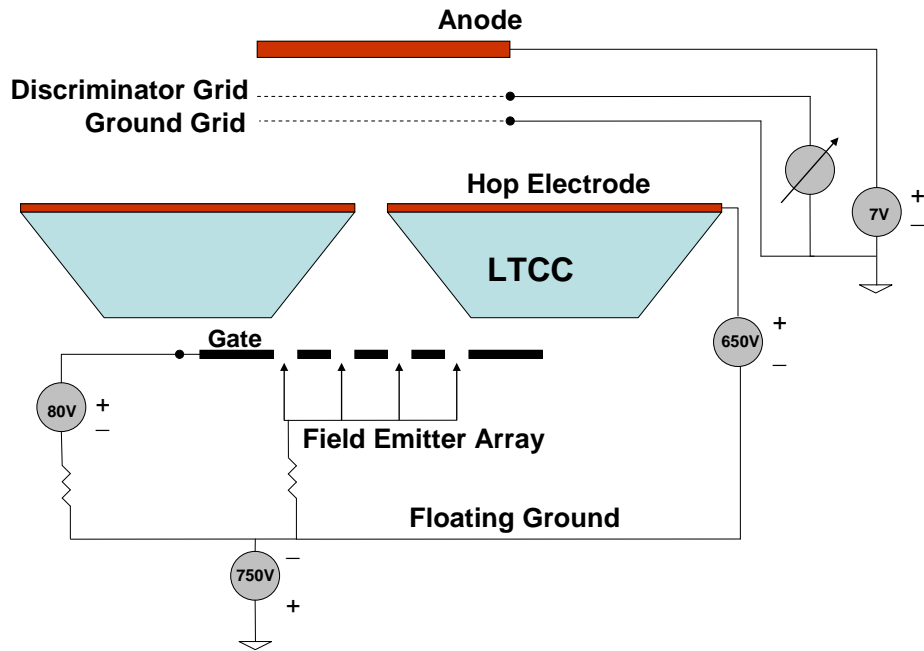


Figure 34. Hop funnel experimental schematic showing energy analyzer measurements.

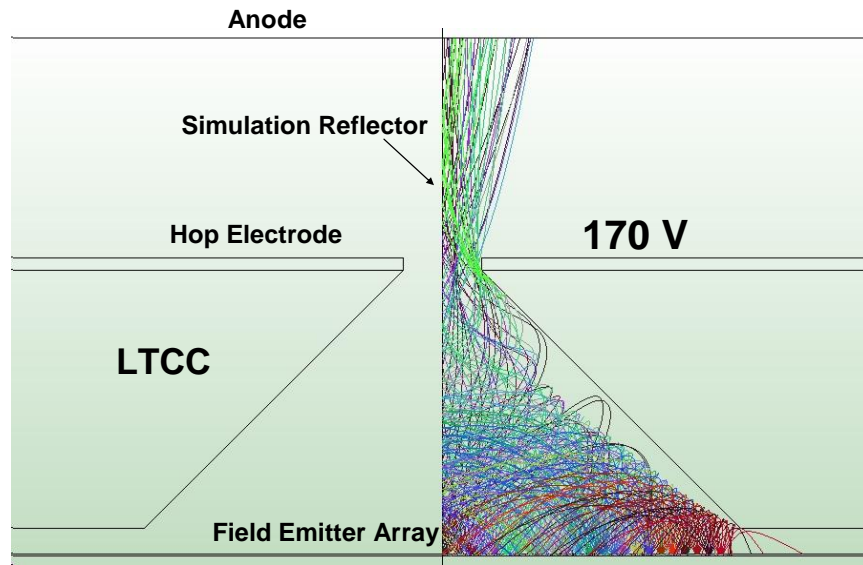


Figure 35. Lorentz simulation of the hop funnel with $V_{hop} = 170$ V where most electrons do not escape. Most current is from primary electrons.

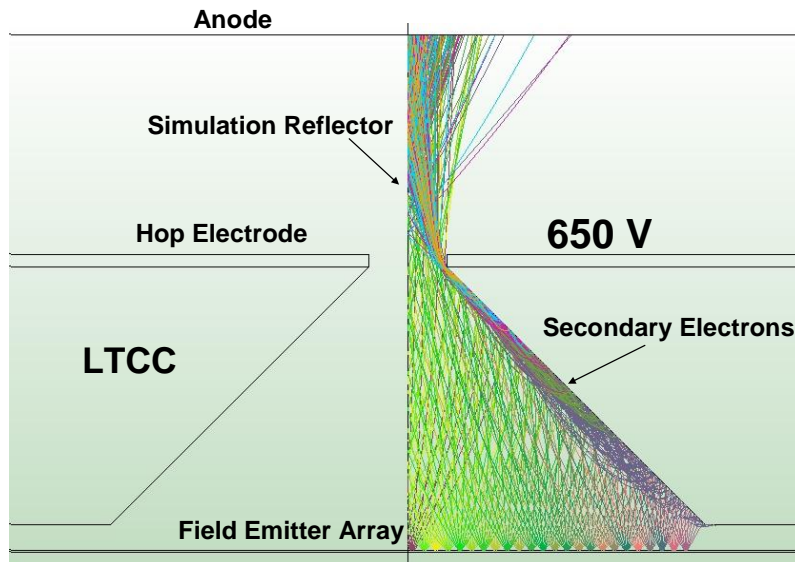


Figure 36. Lorentz simulation of the hop funnel with $V_{hop} = 650$ V where electrons escape.

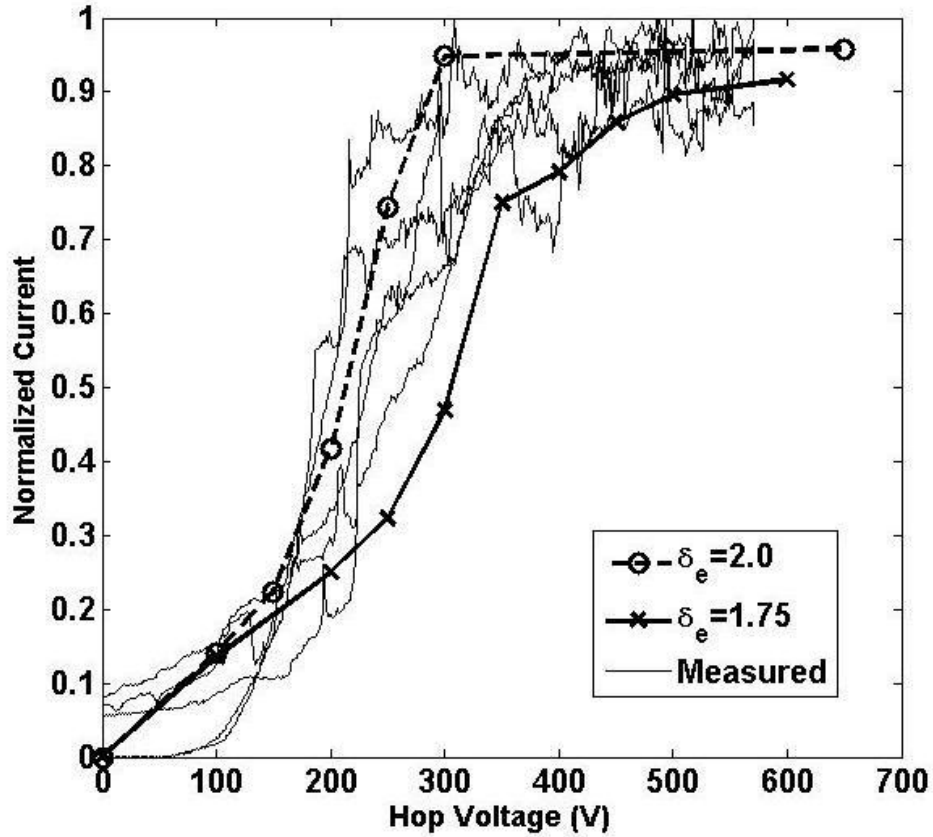


Figure 37. Measured and simulated I-V curves for $W_m=450$ eV

In the performed simulations, the wall of the hop funnel would start uncharged. At each hop funnel electrode voltage, the emission would be injected into the funnel with the virgin wall surface. The simulation was then run until steady state where the current exiting the funnel remained relatively constant. However, the hysteresis in the experimental results could not be simulated. Initially, charging on the bottom of the hop funnel was expected as the cause, but experiments with metal on the funnel bottom ruled out that cause. Charging on the FEA dielectric could be a cause, but experiments require cathodes with charge bleed layers, and those are not available. It was proposed that the charging could be an artifact of the funnel IV sweep itself. So it was decided to change how the simulations were run. Instead of starting with an uncharged hop wall for each hop voltage, the final wall charge from the prior hop voltage simulation would be used as the initial wall charge. This technique would allow the starting conditions to be different as the voltage was ramped up versus when the voltage was ramped down. The results indeed showed an IV hysteresis from the simulation. Shown in Fig. 39 are the IV curves from the simulation when the voltage is ramped up, back down, and back up again all using the surface charge from the prior voltage step. The results very clearly show a hysteresis in the I-V curves.

When the voltage is ramped up the first time, the curve is nearly linear until unity gain. Then saturation occurs. When the voltage is ramped down, the current is flat or decreasing slightly until 200 V. When the voltage steps from 200 V to 175 V, a very clear knee is seen. Note that to fit this data, the secondary emission parameters had to be changed. The first cross over energy was dropped to 40 eV from 70 eV by using the secondary parameters in the code. Otherwise, unity gain was not achieved until 900 V which was well beyond the experimental values.

To demonstrate what occurs at the knee on the ramp down, images at 4 voltage steps down are shown in Fig. 40. As can be seen, at the transition from 200 V to 175 V, there are no longer secondary electrons from near the bottom of the funnel escaping. The secondaries (non-yellow) only occur near the top of the funnel while many of the primaries (yellow) are turned back.

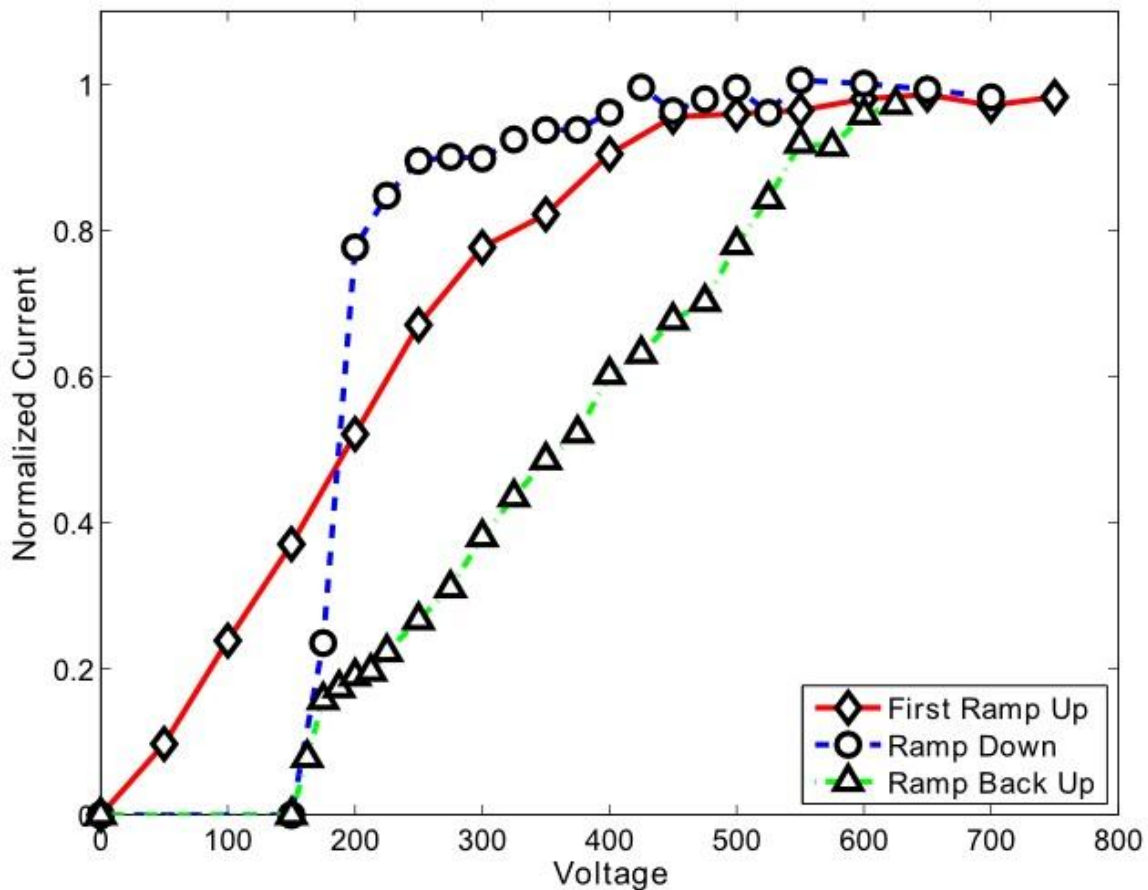
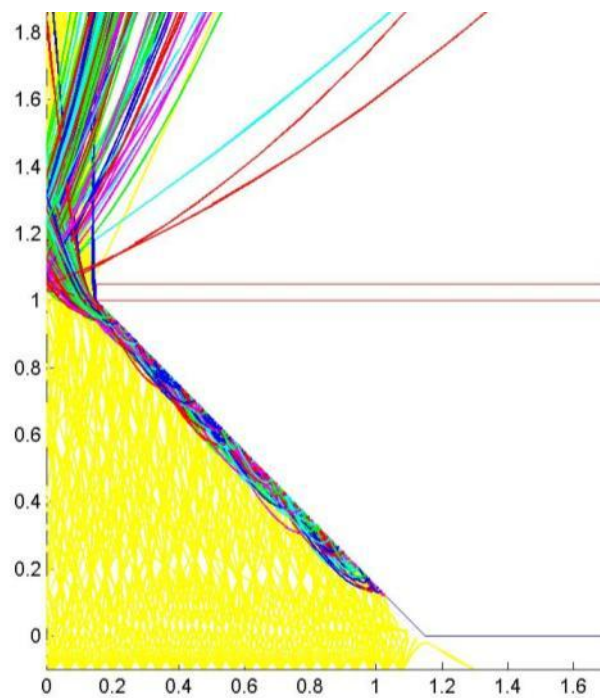
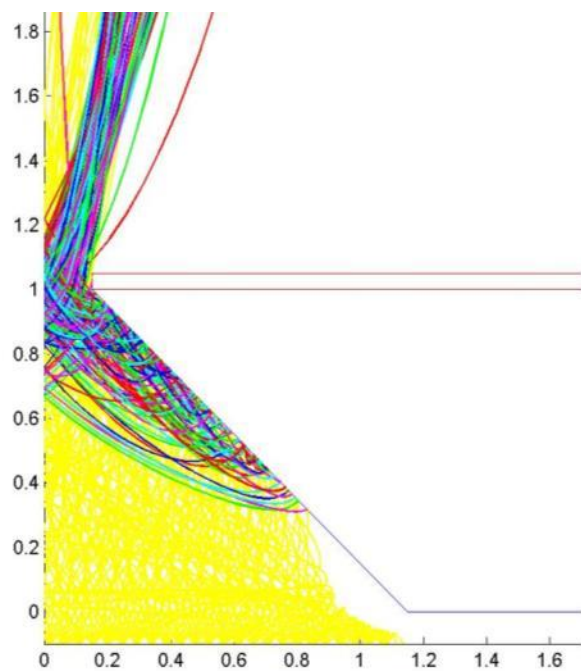


Figure 38. Lorentz2E simulations of the hop IV curves where each voltage step uses the wall surface charge from the prior voltage simulation.



(a) $V_{\text{hop}} = 600 \text{ V}$



(b) $V_{\text{hop}} = 200 \text{ V}$

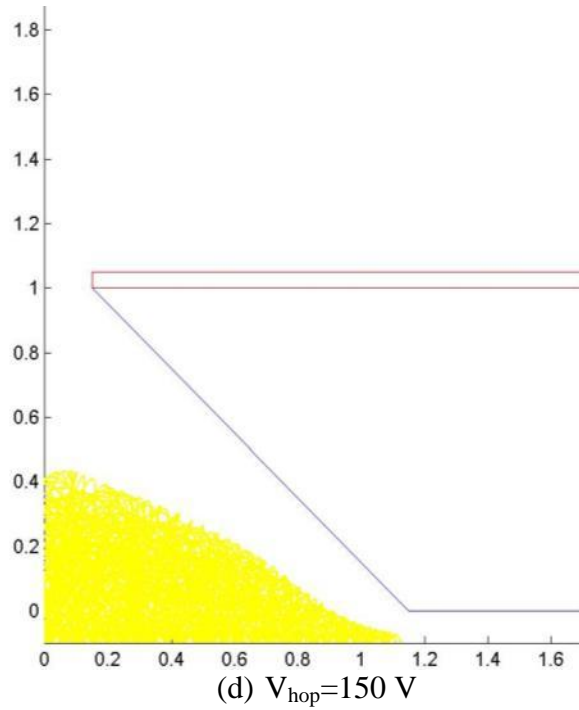
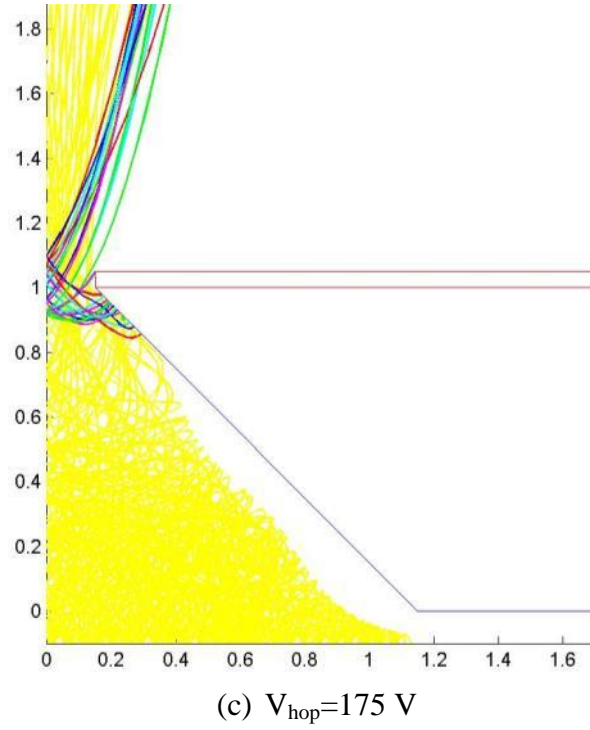


Figure 39. Simulations of the funnel showing the electron rays making the transition from unity gain to low current at the knee of the IV curve with (a) $V_{\text{hop}}=600 \text{ V}$, (b) $V_{\text{hop}}=200 \text{ V}$, (c) $V_{\text{hop}}=175 \text{ V}$, and (d) $V_{\text{hop}}=150 \text{ V}$. The primary rays are in yellow, and the secondaries are in other colors.